Classification: BIOLOGICAL SCIENCES; Cell Biology

# Directional memory arises from long-lived cytoskeletal asymmetries in polarized chemotactic cells

Harrison V. Prentice-Mott[1,2,3,+], Yasmine Meroz[3,+], Andreas Carlson[3], Michael A. Levine[1,2,5], Michael W. Davidson[7], Daniel Irimia[4], Guillaume Charras[6], L. Mahadevan[3,8,9,*] and Jagesh V. Shah[1,2,*]

[1]*Department of Systems Biology, Harvard Medical School, Boston, MA, USA*
[2]*Renal Division, Brigham and Women's Hospital, Boston, MA, USA*
[3]*Paulson School of Engineering and Applied Sciences, Harvard University, Cambridge MA, USA*
[4]*Department of Surgery, Massachusetts General Hospital, Boston, MA, USA*
[5]*Biophysics Graduate Program, Harvard University, Cambridge, MA, USA*
[6]*London Centre for Nanotechnology and Department of Cell and Developmental Biology, University College London, London, United Kingdom*
[7]*National High Magnetic Field Laboratory, Florida State University, Tallahassee, FL, USA*

[8] *Departments of Physics, and Organismic and Evolutionary Biology, Harvard University, Cambridge MA, USA*
[9] *Kavli Institute for Nanobio Science and Technology, and Wyss Institute for Bioinspired Engineering*

[+]these authors contributed equally

[*]Corresponding Authors:

Jagesh V. Shah (designate)
4 Blackfan Circle, HIM 568, Boston, MA
E: Jagesh_shah@hms.harvard.edu
P: (617) 525-5912

L. Mahadevan
322 Pierce Hall, 29 Oxford Street, Cambridge, MA
E: lm@seas.harvard.edu
P: (617) 496-9599

Keywords: Chemotaxis, Moesin, Microtubules, Microfluidics, Directional memory, Cell polarization, Confined cell migration

Running Title: Directional memory in chemotactic cells

Characters: 59,426 chars (no spaces, inc. legends, references and materials and methods)

**Abstract**

Chemotaxis, the directional migration of cells in a chemical gradient, is robust to fluctuations associated with low chemical concentrations and dynamically changing gradients as well as high saturating gradients. Although a number of reports have identified cellular behavior consistent with a directional memory that could account for behavior in these complex environments, the quantitative and molecular details of such a memory process remain unknown. Using microfluidics to confine cellular motion to a one-dimensional channel and control chemoattractant exposure, we observed directional memory in chemotactic neutrophil-like cells. We modeled this directional memory as a long-lived intracellular asymmetry that decays slower than observed membrane phospholipid signaling. Measurements of intracellular dynamics revealed that moesin at the cell rear is a long-lived element that when inhibited results in a reduction of memory. Inhibition of ROCK, downstream of RhoA, stabilized moesin and directional memory. Depolymerization of microtubules (MTs) disoriented moesin deposition and also reduced directional memory. Long-lived polarized cytoskeletal structures, specifically moesin, actomyosin and MTs, provide a directional memory in neutrophil-like cells. (167 words)

**Significance statement**

Cells orient their motility along chemical gradients using sensitive measurements of the external environment, a process termed chemotaxis. How cells are able to sense, respond to and remember varying environmental stimuli is only just beginning to be understood. Here we identify a directional memory in chemotactic neutrophil-like cells. This memory allows cells to orient in low signal gradients and even uniform environments. This memory can be modeled by distinct timescales of chemical sensing and cytoskeletal dynamics, pointing to a general strategy of separating timescales for robust behavioral dynamics in cellular systems. Disrupting specific long-lived molecular assemblies erases directional memory. These studies reveal a novel directional memory resulting from distinct molecular timescales and contributing to chemotactic robustness observed in migrating cells. (120 words)

## Introduction

Directed cell motion underlies important functions in development, immunology and resource foraging [1]. The local cues for cellular orientation are chemical, either in the form of soluble gradients or substrate-bound moieties [2, 3], or physical, in the form of pressure, substrate adhesion etc [4, 5]. In either case, chemical cues activate signaling at the cell surface and are integrated within the cell cytoplasm to give rise to a polarization in the direction of the local gradient. While these processes have been the subject of detailed experimental study and theoretical and computational modeling, the mechanisms by which this orientation is achieved and maintained in the face of environmental noise remains incomplete.

Although migration might be thought of as being very sensitive to the variations in the external environment, instead we see robust migration in a variety of fluctuating environments. These observations all point to the existence of a directional memory in chemotactic cells –a biochemical pathway that stores information about cellular orientation and prevents its loss in the face of fluctuations, transient loss of polarization or saturation of the receptors. For example, recent work has demonstrated memory-based behavior in *Dictyostelium* amoebae under fluctuating waves of chemoattractant [6, 7], although they do not identify potential molecular elements that store this information.

Here we use microchannel-based microfluidic devices to observe membrane and cell polarization and movement in confined mammalian leukocyte-like cells. Cells in this environment exhibit a strong bias to repolarize in the previous direction of motion after a period of depolarization, in the absence of a strong gradient. This memory is time-dependent and decays when the cell is unstimulated. To describe these results, we construct a minimal phenomenological model coupling membrane and cytoskeletal polarization and show that it suffices as a memory by separating the timescales for the decay of membrane and cytoskeletal polarization. To understand how this might be achieved, we look at putative molecular mechanisms and show that the cytoskeletal ERM family protein moesin has a long turnover time, in comparison to membrane phospholipid signaling and that moesin inhibition results in a loss of memory. Depolymerization of microtubules also disrupts memory, but by disrupting moesin localization, or re-orienting the potential memory element. Together, our experimental and theoretical models show that this membrane-cytoskeletal system acts to keep cells biased in their orientation based on previous signaling history and may act to drive directed motility in noisy gradients.

## Results

We adapted microfluidic devices that confine cell migration to a one-dimensional geometry to allow independent and controlled exposure of chemoattractant to each side of the cell (Figure S1A) [5, 8].

Cells enter microchannels that connect two external reservoirs that maintain chemoattractant concentrations at each end. The microchannels are small enough (3 μm x 5 μm) that a single cell fills the cross-sectional area of the channel and acts as a barrier for fluid flow and diffusion, maintaining the concentration difference across the cell (Figure S1A). Thus, the cell senses differences between chemoattractant concentrations across it and motion is restricted to 1-D (up and down the channel). Moreover, the chemical exposure and cell geometry remain constant while the cell confinement is maintained irrespective of cell motion, thus creating a stable fixed difference across the cell.

We subjected HL-60 (neutrophil-like) [9] cells to chemoattractant differences in fMLP (formylated Met-Leu-Phe). $C_o$ designates the concentration in the lower reservoir (i.e. [lower]) and $\Delta C$ the difference (ie. [upper]-[lower]). For a 0-100 nM difference ($C_o$= 0 nM and $\Delta C$ = 100 nM) cells showed strong polarization towards the higher fMLP concentration, as seen by both morphology and the accumulation of Ph-Akt-EGFP at the leading edge of the motile cell (marking PIP3 lipids [10]) (Figure 1A, B). Quantitative analysis of cell polarization [11] and motility showed persistence in both measures (see SI) for all cells measured (Figure 1C). When cells were exposed to a smaller difference, cells were far less persistent in their polarization ($C_o$ = 0 nM, $\Delta C$ = 3 nM, Figure 1D, E). Quantitative analysis of cell polarization and motility showed fluctuations in both measures (Figure 1F). The value 3 nM was chosen because it is well below the equilibrium dissociation constant ($K_d$) of the ligand fMLP for its receptor (10-15 nM) [12]. Notably, cells that lose polarization exhibit a small motion opposite to their original direction of motion, a relaxation of its morphology, not a directed motion. Under saturating conditions ($C_o$ = 50 nM, $\Delta C$ = 50 nM) where the background concentration of 50 nM is well above the receptor-ligand $K_d$ (Figure S1B, C) we observed polarization persistence and directional changes similar to those seen for small differences (Figure S1D).

Chemotactic cells can also undergo spontaneous polarization and motility in the absence of an external gradient, usually due to activation by extracellular matrix components such as fibronectin [13, 14]. Observation of cells in 0-0 environments ($C_o$ = 0 nM, $\Delta C$ = 0 nM) revealed cells with frequent switching of orientation and very few cells that maintained persistence across the entire channel (Figure 1G, H, I). When cells were placed in uniform environments of higher concentrations we observed an increased level of persistent cells at 3 nM ($C_o$ = 3 nM, $\Delta C$ = 0 nM, Figure S1E, F and G) that increased at 10 nM ($C_o$ = 10 nM, $\Delta C$ = 0 nM, Figure S1H, I and J) and then dropped at 100 nM ($C_o$ = 100 nM, $\Delta C$ = 0 nM, Figures S1K,L and M).

To quantify the polarization dynamics we derived histograms of instantaneous cell polarization combining many cell trajectories (Figures 2A and S2). All histograms show peaks near -1 and 1, reflecting the polarized state in both directions, and a small enrichment at 0 (the unpolarized state). The sign of the polarization was chosen such that the initial direction of polarization was positive. For

persistently polarized cells, as observed in strong chemotactic differences (e.g. $C_o$ = 0 nM, $\Delta C$ = 100 nM), cells exhibited a strong polarization bias toward +1 (Figure S2A). At low chemoattractant differences (eg. $C_o$ = 0 nM, $\Delta C$ = 3 nM) we also observed a bias in polarization to the original direction of polarization with some fluctuation (Figure S2B). This was also seen for differences on a large background concentration (eg. $C_o$ = 50 nM, $\Delta C$ = 50 nM, Figure S2C). Histograms of cell polarization in uniform environments ($\Delta C$ = 0 nM) revealed that cells in 3 nM and 10 nM also showed a non-zero bias (Figure 2A, B). In the absence of chemoattractant (0 nM) and at 100 nM uniform concentration, the mean polarization moved closer to 0 perhaps indicating saturation (Figures 2A and S2G). The mean and skewness (a measure of asymmetry) of these distributions indicated a directional bias under both chemotactic differences and uniform conditions (Figure 2C).

To understand this bias in uniform environments we revisited the trajectories of single cells. A cell that re-polarized in the original direction of polarization after the depolarization event was designated a "same" cell, whereas cells that re-polarized in the opposite direction were designated as "switched". In environments with a chemical difference, cells exhibited a strong bias towards same (non-switching) behavior (Figure 2D). In some uniform environments cells also exhibited strong non-switching behavior indicating a memory of the previous direction (eg. 3 nM and 10 nM) whereas there was little to no bias in other uniform environments (eg. 0 nM and 100 nM). While the bias in the chemical difference environments might be expected, the bias seen in uniform environments, specifically 3 nM and 10 nM (~80%, $p<0.004$, Fisher exact test), indicated that internal cellular factors can determine the direction of re-polarization and not the external conditions.

To investigate the temporal dynamics of this memory, we used a dynamic environment to shift cells from a uniform environment with chemoattractant ($C_o$ = 10 nM, $\Delta C$ = 0 nM) to one with none ($C_o$ = 0 nM, $\Delta C$ = 0 nM) to promote depolarization at a specified time (Figure 3A). Chemoattractant was then re-introduced after a time delay. The majority of cells depolarized under removal of the chemoattractant (69/77, 90%, Figure S3A) exhibiting both chemical (PH-Akt-GFP) and morphological depolarization. After two minutes in the absence of chemoattractant, a uniform environment ($C_o$ = 10 nM, $\Delta C$ = 0 nM) was re-established. Unpolarized cells re-exposed to the uniform environment repolarized either in the same direction (Figure 3B) to their previous motion or switched (Figure 3C). Cells re-exposed after two minutes of no chemoattractant exhibited a 90% bias towards the original direction (Figure 3D). When extended out to 10 minutes of no chemoattractant the bias dropped to 70%. During the 10 minute depolarization time, many cells spontaneously polarized prior to the reintroduction of chemoattractant (29/65, 45%, Figure S3A) and their directional bias towards the initial direction of polarization was ~80% (marked "Spontaneous" in Figure 3D) indicating that the re-addition of chemoattractant was not required to activate the polarization machinery but that the memory was still intact. Interestingly, a small number of cells (8/77, 10%) did not depolarize after

removal of the chemokine indicating some long-lived persistence in the absence of an external signal. We investigated the role of cell position in the channel given that some cells would experience differential temporal cues (front vs. back) if they were closer to the channel ends. We found no correlation between the position in the channel and choice of polarization direction (Figure S3B).

The polarization direction after re-exposure to the uniform environment was biased by previous orientations via the directional memory, but we expected that strong chemoattractant differences in the opposite direction would be capable of overcoming this memory. We modified the dynamic protocol to take cells from the no chemoattractant environment to a fixed difference ($C_o$ = 10 nM, $\Delta C$ = -10 nM) and found that for those cells initially polarized in the opposite direction to the final difference, 90% of the cells switched direction upon re-polarization in the direction of the imposed difference (Figure 3D, "Forced").

To quantify these observations in a minimal representation that accounts for the directional memory we developed a phenomenological model for polarization dynamics as a function of the difference in concentration across the cell $\Delta C$ and the average concentration $C_o + \Delta C/2$. Our mathematical model represents the migrating cell as a composite of two interacting systems – a sensing unit embedded in the membrane and an actuating motor unit embedded in the cytoskeleton. The cytoskeleton can only indirectly sense the environment through the polarization state of the membrane, however the cytoskeletal polarization biases membrane polarization much like the external environment does. We denote the membrane polarization by $p_m(t)$ as measured by PH-Akt-GFP activity, and the cytoskeleton polarization by $p_c(t)$. Both these variables averaged across the cell can take values in the range [-1,1] where positive and negative values represent polarized states and a vanishing value represents an unpolarized state. The dynamics of the system is modeled by a pair of Langevin-like equations for the membrane and cytoskeletal polarization, using a double well potential that characterize the two polarized states separated by an unpolarized state (Figure 4A) and symmetry considerations:

**Eq(1) a** $$dp_m/dt = -\alpha_m p_m (p_m-1) (p_m+1) + | \alpha_m |(\Delta n + p_c)+ \eta_m$$

**b** $$dp_c/dt = -\alpha_c p_c (p_c-1) (p_c+1) + | \alpha_c |p^*_m+ \eta_m$$

The first term on the r.h.s. arises from the derivative of the double well potential, with three steady states corresponding to $p_m$, $p_c$=0,+1,-1 (Figure 4Ai, ii). Here $\alpha_m$ and $\alpha_c = \alpha_c(\alpha_m)$ are the stochastic gains for the membrane and cytoskeleteon (which are functions of C via the fraction of bound receptors), so that for $\alpha_m$ , $\alpha_c$ <0, the unpolarized state is the only stable state, while for $\alpha_m$, $\alpha_c$ >0, there are two stable states $p_m$, $p_c$=+1 and $p_m$, $p_c$=-1 corresponding to polarization in the initial and opposite direction respectively. A gradient in the chemokine concentration biases the preferred polarization. This corresponds to the term $\Delta$ n, the difference in the fraction of bound receptors, which breaks the symmetry of potential landscape with a deeper well associated with the preferred

polarization (Figure 4Aiii). $\eta_m(t)$ is uncorrelated Gaussian. The second term in Eq. 1b denotes the time averaged membrane polarization $p^*_m(t) = \int^t_{-\infty} p_m(t)\,\Gamma(t-\tau)d\tau \,/\, \int^t_{-\infty} \Gamma(t-\tau)d\tau$, with $\Gamma(t) = Ae^{-t/\tau}$ denoting a memory kernel associated with the signaling cascade from the membrane to the cytoskeleton; with a characteristic time $\tau$ . It has been observed that if the membrane depolarizes and repolarizes after a given time, it will repolarize in the direction dictated by the cytoskeletal polarization. This suggests a minimal coupling where the integration of the membrane polarization over time that biases $p_c$ in the same direction, in turn biasing $p_m$ again (see SI for Model Description) .Eq. (1) together with a stochastically varying gain $\alpha_m$ (subject to receptor binding constraints – see SI) form a complete set of equations for the dynamics of membrane and cytoskeleton polarization for some given initial conditions, with a single dimensionless parameter that controls the dynamical processes – $\tau\,\alpha_m$.

To gain some intuition about the model, we first look at the case $\tau = 0$, effectively decoupling $p_m$ and $p_c$. Figure 4B shows examples of simulated trajectories of $p_m(t)$ . Since $\alpha_m$ is a function of the rate of binding events and noise, it to respond to external conditions, switching between polarization directions, and between polarized and unpolarized states. Next, we introduce memory with non-zero $\tau$ that couples $p_m$ and $p_c$, and we carry out simulations following the direction in which a cell re-polarizes following a depolarization event. In the absence of any chemokine, simulated cells exhibited no bias in the re-polarization direction (Figure 4C), while the introduction of even a small concentration difference resulted in a measurable bias, which increased with the magnitude of $\Delta n$. Figure 4D shows that we qualitatively reproduce experimental behavior. In addition, cells in a uniform $C_o$ also exhibited a directional bias, (absent for $\tau = 0$). These simulations also recovered distributions of instantaneous polarization (Figure S4). Simulations of dynamic removal and re-introduction of chemokine (as in Figure 3A) showed a strong bias to repolarizing in the same direction as the original polarization (Figure 4D). Increasing the time for re-introduction of chemokine decreased the fidelity of the directional "memory" (Figure S4E). Increasing $\tau$, which simulates longer cytoskeletal timescales, resulted in a longer-lived directional memory.

Our model also naturally allows us to explain seemingly paradoxical behaviors observed in other chemotactic systems. Indeed in In *Dictyostelium* Nakajima et al [9] showed that the speed of waves of chemoattractant affect the migration behavior, dubbing this the "wave-paradox"; for fast waves no migration is observed, for slow waves cells move towards the incoming wave but reverse their direction as the wave passes the cell, while for intermediate wave velocities cells migrate towards the incoming wave throughout the wave cycle, resulting in forward cell migration in a negative chemotactic gradient. We now turn to describe this phenomenon using our two-layered mathematical model. We define two timescales in these experiments; $\tau_{\Delta n}$ the timescale of the positive gradient (half the time the wave needs to cross the cell), and $\tau_{pc}$ the timescale of the memory kernel. As the wave comes in, it imposes a

positive gradient $\Delta n>0$ while $p_c=0$, therefore the total bias is positive and $p_m$ increases with time to its maximum value +1. The temporal integration of $p_m$ biases $p_c$, which therefore increases. After the wave passes the cell, the external gradient switches sign, i.e. $\Delta n \rightarrow -\Delta n$. For slow waves, i.e. $\tau_{\Delta n} > \tau_{pc}$ , upon switching of the gradient $p_c$ will have already reached its maximum value, and therefore the total bias ($-\Delta n + p_c$) effectively diminishes with time and eventually switches signs, i.e. $p_m$ also switches signs (Figure S4F). For intermediate waves, i.e. $\tau_{\Delta n} \sim \tau_{pc}$ , upon switching of the gradient $p_c$ has not reached its maximum value yet and is still increasing, effectively canceling out the negative bias of the gradient $-\Delta n$, i.e. $p_m$ does not switch signs (Figure S4G). As with previous work in *Dictyostelium* [6, 7], which utilizes the more complex LEGI+M model, our model explains both directional memory and the wave paradox. We point out that the main differences lay in the reduced complexity of our model. In particular, our holistic model led us to three equations that characterize the dynamics of the observable chemical polarization of the membrane $p_m$ , the mechanical polarization of the cytoskeleton $p_c$, as well as the gain associated with chemokine binding $\alpha$, permitting the identification of putative cellular components corresponding to these variables. The model is subject to six parameters which depend on the environment: $k_D$, the dissociation rate, $k_+$ the association rate, $\eta$ and $\eta_\alpha$ the magnitude of noise, the minimal bounds for $\alpha$ and lastly $\tau$, the extent of the memory kernel.

Two molecular assemblies that might serve as repositories of this long-lived asymmetry driving directional memory are the actomyosin network and the ERM-actin-membrane structures that localize to the rear of a polarized cell [15, 16]. Both structures have been previously shown to exhibit turnover times that are long compared to PH-Akt dynamics in other cell types [17, 18]. We introduced mApple-fusions to myosin light chain (MLC) and moesin into PH-Akt-GFP expressing HL-60 cells. Polarization decay of mApple-MLC, after chemoattractant removal, was similar to that of PH-Akt-GFP (Figures 5A, S5A, 5B and S5C). Unlike MLC, the mApple-moesin remained polarized longer than PH-Akt-GFP, after chemoattractant removal, indicating longer-lived asymmetry within the cell (Figures 5C, S5B, 5D and S5C). While the decay rate was only slightly faster, the most obvious difference was the delay in moesin depolarization, which results in a rapid increase in the cumulative difference between moesin and PH-Akt polarization compared to MLC vs. PH-Akt (Figure S5C).

Moesin is a member of the ERM (Ezrin, Radixin, Moesin) family of proteins that acts to connect the plasma membrane (via polyphosphatidyl-inositol lipids) to the cortical actin cytoskeleton [19-21]. A critical Threonine residue is present in the C-terminus of each of the ERM family members that regulates their interaction with f-actin and the N-terminal FERM (Band4.1, Ezrin, Radixin, Moesin) domain regulates an interaction with microtubules [22]. A quinolone-based compound (NSC668394) was previously developed to bind this threonine and prevent its phosphorylation, disrupting f-actin binding [23]. Addition of NSC668394 at 50 μM to the dynamic protocol (during the no

chemoattractant phase) resulted in a reduction of directional memory from 90% to 60% (Figure 5E). Blebbistatin, a myosin II inhibitor (50 μM) also decreased directional memory [24].

The ROCK kinase is a downstream effector of Rho-GTP, an integrator of the back domain [25], and its inhibition (via Y27632, 20 μM [26]) did not decrease directional memory (Figure 5E). A significant number of cells under ROCK inhibition and chemoattractant removal continued to move along the channel (Figure S5D). The combination of ROCK and moesin inhibition preserved memory. To understand the interrelationship between these components, we investigated the decay of moesin under each of these drugs. Interestingly, ROCK inhibition stabilized moesin at the back of the depolarized cell independently of PH-Akt (Figure 5F and G). All other treatments had no effect on the decay of moesin (Figure 5H). The addition of the moesin inhibitor to ROCK inhibition partially restored moesin decay dynamics (Figure 5I).

Treatment of chemotactic cells with colcemid (10 μM) a microtubule-depolymerizing compound during the no chemoattractant phase, resulted in the mis-localization of moesin and PH-Akt (Figure S6A and SB) effectively accelerating the decay of moesin polarization and reducing directional memory (Figures 6A and 6B). Addition of the ROCK inhibitor to colcemid resulted in a stabilization of the mis-localized moesin at both the front and back of the cell (Figures S6C and S6D) and thus a reduction of memory (Figures 6A and 6B). This stabilization resulted in a dramatic increase in cells that did not repolarize after the re-introduction of chemoattractant (Figure S6E).

**Discussion**

Observations of chemotactic neutrophil-like cells in a variety of chemical differences and uniform environments revealed a bias in repolarization directions towards that of previous cellular orientations. A model based on long-lived asymmetric cellular elements that persist after cells have depolarized and that influence orientation upon repolarization was able to recapitulate many aspects of this memory.

Observations of internal dynamics revealed that moesin is a strong candidate for this memory since it has the requisite long-lived behavior and its inhibition reduces directional memory. While moesin exhibits the long polarization timescale indicative of a directional memory (exhibiting faster decay and delay in depolarization), inhibition via the small quinolone molecule did not change moesin dynamics but did interrupt memory. The action of NSC668394 is to block T558 phosphorylation on moesin and decouple it from f-actin [23]. This decoupling may accelerate the depolarization of the actual memory element. Alternatively, the phosphosite itself may act to bias repolarization [27].

Blebbistatin also reduced memory, thereby implicating myosin as a potential memory element. This was surprising given that MLC polarization decay did not exhibit the appropriate time scale to account for the observed directional memory (as shown in Figures 5B and S5C). However, it should be noted that MLC (specifically the regulatory light chain) is a marker of myosin contractile activity and not necessarily one of myosin localization. It is possible that myosin heavy chain localization remains polarized on a longer time scale than does the polarization of the contractile activity. Recent work identifying a serine-rich motif in myosin heavy chain II-B in regulating cell polarization makes this a good candidate [28]. Under ROCK inhibition moesin and likely myosin were stabilized thereby promoting memory indicating a link between RhoA activity and moesin turnover [29]. However, the combination of ROCK and moesin inhibition restored moesin decay dynamics but still exhibited some memory supporting a role for actomyosin.

Microtubule disruption also reduces directional memory but by mislocalizing moesin rather than accelerating its decay from the cell membrane. Loss of MTs in neutrophils has been previously associated with loss of polarity and reduced directional migration [30]. Here we propose that the role of MTs acts to focus biochemical activities to maintain proteins such as moesin (and myosin) at the back domain, as has been observed in other cell types [31]. One candidate for this regulation would be the RhoA GTPase that has been linked to MTs through the MT-bound RhoGEF, GEF-H1 [32].

Together these data support a model of cellular orientation that depends on both external environmental cues and internal membrane that polarize long-lived cytoskeletal markers that act as a form of directional memory. Models which focus only on the early chemotactic response associated with membrane polarization, e.g. LEGI would be unaffected by cytoskeletal perturbations. Our observations under perturbations of moesin and myosin show that this is not the case supporting our model that couples the dynamics of cytoskeletal and membrane polarizations.

Further dynamical tests in confined geometries and 2-D chemotactic fields should help refine the layered model and account for additional time and length scales associated with complex spatiotemporal signaling (e.g. small GTPases [15]) within the cell. For example, the model predicts that when the new external cue is aligned with the internal memory it may establish polarization more rapidly than when an external cue is oriented in opposition to the internal memory. Another prediction is that altering the relaxation of the cytoskeleton should also alter the temporal extent of the memory kernel. Such kinetic measurements would begin to dissect inter-process timescales and explain behaviors such as U-turns originally described by Zigmond and colleagues [33] that occur at slow changes in the external environment but disappear in rapidly changing gradients [34] and maintain polarity in the face of reversed chemoattractant gradients [35]. More generally, our study shows how the temporal separation of membrane and cytoskeletal polarization allows a cell to sense and respond to a fluctuating environment relatively robustly.

## Experimental Procedures

### Cell Culture and Stable Line Production:

HL-60 cell lines were generated and maintained as previously described [5], with details in the SI. Dual expression cell lines were generated via lentiviral infection of cells stably expressing PH-Akt-GFP with either MLC-mApple or hsMoesin-mApple.

### Microfluidic Device Operation:

Operation of the microfluidic devices was carried out as previously described [5, 8] with details available in the SI. To expose cells to dynamic changes in concentration, cells were loaded and allowed to enter the microchannels in a uniform concentration of 10 nM fMLP by clamping off the 0 nM reservoir. The chemokine was then washed away by clamping off the 10 nM inlet and releasing the 0 nM reservoir. Chemokine was reintroduced by clamping the 0 nM inlet and releasing the 10 nM inlet. Inhibitors were added to the 0 nM reservoir (see SI).

### Image Acquisition and Analysis:

The cell polarization was determined using a clustering method similar to that described by Ku et al. [11] with details in the SI. To determine cell persistence, cells that maintained a polarized morphology and a polarization parameter > 0.8 (the threshold) throughout the entire length of the channel, or during the entire period of imaging were determined to be persistent. Transient fluctuations of the polarization parameter below the threshold for a single frame were still determined to be persistent. In the case that the polarization parameter remained below the threshold for 2 or more frames the cell was determined to have depolarized. Repolarization occurred it the polarization parameter increased above the threshold and a morphological polarization was established.

**Acknowledgements**

The authors thank the Shah and Mahadevan lab members and Tim Mitchison for valuable discussions. Microfabrication work was supported by the BioMEMS resource center (P41 EB002503). This work was supported from the BBSRC (BB/F021402) to GC and Brigham and Women's Renal Division funds to JVS, and a MacArthur Fellowship to LM. Yasmine Meroz, is an Awardee of the Weizmann Institute of Science – National Postdoctoral Award Program for Advancing Women in Science.

## References


1. Swaney, K.F., Huang, C.-H., and Devreotes, P.N. (2010). Eukaryotic chemotaxis: a network of signaling pathways controls motility, directional sensing, and polarity. Annual review of biophysics *39*, 265-289.
2. Zigmond, S.H. (1974). Mechanisms of sensing chemical gradients by polymorphonuclear leukocytes. Nature *249*, 450-452.
3. Brandley, B.K., and Schnaar, R.L. (1989). Tumor cell haptotaxis on covalently immobilized linear and exponential gradients of a cell adhesion peptide. Developmental Biology *135*, 74-86.
4. Lo, C.-M., Wang, H.-B., Dembo, M., and Wang, Y.-l. (2000). Cell Movement Is Guided by the Rigidity of the Substrate. Biophysical Journal *79*, 144-152.
5. Prentice-Mott, H.V., Chang, C.-H., Mahadevan, L., Mitchison, T.J., Irimia, D., and Shah, J.V. (2013). Biased migration of confined neutrophil-like cells in asymmetric hydraulic environments. Proc Natl Acad Sci U S A *110*, 21006-21011.
6. Skoge, M., Yue, H., Erickstad, M., Bae, A., Levine, H., Groisman, A., Loomis, W.F., and Rappel, W.-J. (2014). Cellular memory in eukaryotic chemotaxis. Proceedings of the National Academy of Sciences of the United States of America, 201412197.
7. Nakajima, A., Ishihara, S., Imoto, D., and Sawai, S. (2014). Rectified directional sensing in long-range cell migration. Nature communications *5*, 5367.
8. Irimia, D., Charras, G., Agrawal, N., Mitchison, T., and Toner, M. (2007). Polar stimulation and constrained cell migration in microfluidic channels. Lab Chip *7*, 1783-1790.
9. Millius, A., and Weiner, O.D. (2009). Chemotaxis in neutrophil-like HL-60 cells. Methods in molecular biology (Clifton, N.J.) *571*, 167-177.
10. Meili, R., Ellsworth, C., Lee, S., Reddy, T.B.K., Ma, H., and Firtel, R.A. (1999). Chemoattractant- mediated transient activation and membrane localization of Akt/PKB is required for efficient chemotaxis to cAMP in Dictyostelium. The EMBO Journal *18*, 2092-2105.
11. Ku, C.-J., Wang, Y., Weiner, O.D., Altschuler, S.J., and Wu, L.F. (2012). Network crosstalk dynamically changes during neutrophil polarization. Cell *149*, 1073-1083.
12. Williams, L.T., Snyderman, R., Pike, M.C., and Lefkowitz, R.J. (1977). Specific receptor sites for chemotactic peptides on human polymorphonuclear leukocytes. Proceedings of the National Academy of Sciences of the United States of America *74*, 1204-1208.
13. Li, L., Nørrelykke, S.F., and Cox, E.C. (2008). Persistent cell motion in the absence of external signals: a search strategy for eukaryotic cells. PLoS ONE *3*, e2093.
14. Bosgraaf, L., and Van Haastert, P.J.M. (2009). Navigation of chemotactic cells by parallel signaling to pseudopod persistence and orientation. PLoS ONE *4*, e6842.
15. Xu, J., Wang, F., Van Keymeulen, A., Herzmark, P., Straight, A., Kelly, K., Takuwa, Y., Sugimoto, N., Mitchison, T., and Bourne, H.R. (2003). Divergent signals and cytoskeletal assemblies regulate self-organizing polarity in neutrophils. Cell *114*, 201-214.
16. Seveau, S., Keller, H., Maxfield, F.R., Piller, F., and Halbwachs-Mecarelli, L. (2000). Neutrophil polarity and locomotion are associated with surface redistribution of leukosialin (CD43), an antiadhesive membrane molecule. Blood *95*, 2462-2470.
17. Wang, Y., Ku, C.-J., Zhang, E.R., Artyukhin, A.B., Weiner, O.D., Wu, L.F., and Altschuler, S.J. (2013). Identifying Network Motifs that Buffer Front-to-Back Signaling in Polarized Neutrophils. CellReports *3*, 1607-1616.
18. Fritzsche, M., Thorogate, R., and Charras, G. (2014). Quantitative analysis of ezrin turnover dynamics in the actin cortex. Biophysical Journal *106*, 343-353.
19. Neisch, A.L., and Fehon, R.G. (2011). Ezrin, Radixin and Moesin: key regulators of membrane–cortex interactions and signaling. Current Opinion in Cell Biology *23*, 377-382.
20. Bretscher, A., Edwards, K., and Fehon, R.G. (2002). ERM proteins and merlin: integrators at the cell cortex. Nature Reviews Molecular Cell Biology *3*, 586-599.
21. Kunda, P., Pelling, A.E., Liu, T., and Baum, B. (2008). Moesin Controls Cortical Rigidity, Cell Rounding, and Spindle Morphogenesis during Mitosis. Current Biology *18*, 91-101.

22. Solinet, S., Mahmud, K., Stewman, S.F., Ben El Kadhi, K., Decelle, B., Talje, L., Ma, A., Kwok, B.H., and Carreno, S. (2013). The actin-binding ERM protein Moesin binds to and stabilizes microtubules at the cell cortex. The Journal of Cell Biology *202*, 251-260.
23. Bulut, G., Hong, S.H., Chen, K., Beauchamp, E.M., Rahim, S., Kosturko, G.W., Glasgow, E., Dakshanamurthy, S., Lee, H.-S., Daar, I., et al. (2011). Small molecule inhibitors of ezrin inhibit the invasive phenotype of osteosarcoma cells. Oncogene *31*, 269-281.
24. Straight, A.F., Cheung, A., Limouze, J., Chen, I., Westwood, N.J., Sellers, J.R., and Mitchison, T.J. (2003). Dissecting temporal and spatial control of cytokinesis with a myosin II Inhibitor. Science (New York, NY) *299*, 1743-1747.
25. Wong, K., Pertz, O., Hahn, K., and Bourne, H. (2006). Neutrophil polarization: spatiotemporal dynamics of RhoA activity support a self-organizing mechanism. Proc Natl Acad Sci USA *103*, 3639-3644.
26. Uehata, M., Ishizaki, T., Satoh, H., Ono, T., Kawahara, T., Morishita, T., Tamakawa, H., Yamagami, K., Inui, J., Maekawa, M., et al. (1997). Calcium sensitization of smooth muscle mediated by a Rho-associated protein kinase in hypertension. Nature *389*, 990-994.
27. Liu, X., Yang, T., Suzuki, K., Tsukita, S., Ishii, M., Zhou, S., Wang, G., Cao, L., Qian, F., Taylor, S., et al. (2015). Moesin and myosin phosphatase confine neutrophil orientation in a chemotactic gradient. The Journal of experimental medicine *3*, 586.
28. Juanes-Garcia, A., Chapman, J.R., Aguilar-Cuenca, R., Delgado-Arevalo, C., Hodges, J., Whitmore, L.A., Shabanowitz, J., Hunt, D.F., Horwitz, A.R., and Vicente-Manzanares, M. (2015). A regulatory motif in nonmuscle myosin II-B regulates its role in migratory front-back polarity. The Journal of Cell Biology *209*, 23-32.
29. Ivetic, A., and Ridley, A.J. (2004). Ezrin/radixin/moesin proteins and Rho GTPase signalling in leucocytes. Immunology *112*, 165-176.
30. Xu, J., Wang, F., Van Keymeulen, A., Rentel, M., and Bourne, H.R. (2005). Neutrophil microtubules suppress polarity and enhance directional migration. Proc Natl Acad Sci USA *102*, 6884-6889.
31. Zhang, J., Guo, W.H., and Wang, Y.L. (2014). Microtubules stabilize cell polarity by localizing rear signals. Proceedings of the National Academy of Sciences of the United States of America.
32. Kwan, K.M., and Kirschner, M.W. (2005). A microtubule-binding Rho-GEF controls cell morphology during convergent extension of Xenopus laevis. Development (Cambridge, England) *132*, 4599-4610.
33. Zigmond, S.H., Levitsky, H.I., and Kreel, B.J. (1981). Cell polarity: an examination of its behavioral expression and its consequences for polymorphonuclear leukocyte chemotaxis. The Journal of Cell Biology *89*, 585-592.
34. Irimia, D., Liu, S.-Y., Tharp, W.G., Samadani, A., Toner, M., and Poznansky, M.C. (2006). Microfluidic system for measuring neutrophil migratory responses to fast switches of chemical gradients. Lab Chip *6*, 191-198.
35. Robertson, A.L., Holmes, G.R., Bojarczuk, A.N., Burgon, J., Loynes, C.A., Chimen, M., Sawtell, A.K., Hamza, B., Willson, J., Walmsley, S.R., et al. (2014). A zebrafish compound screen reveals modulation of neutrophil reverse migration as an anti-inflammatory mechanism. Science translational medicine *6*, 225ra229-225ra229.
36. Chung, S.H., and Kennedy, R.A. (1991). Forward-backward non-linear filtering technique for extracting small biological signals from noise. Journal of Neuroscience Methods *40*, 71-86.

**Figure Legends**

Figure 1: **Cellular response to static chemical environments.** (**A-C**) Montages of cells expressing PH-Akt-GFP in the conditions $C_o$=0, $\Delta C$=100 (**A**). Kymograph of cell shown in (**A**), false-colored according to the color bar shown on the left (**B**). Plots of cell centroid and PH-Akt polarization (see Experimental Procedures) for corresponding montage and kymograph (**C**). (**D-F**) Montage (**D**), kymograph (**E**) and plots (**F**) for a cell in the condition $C_o$=0, $\Delta C$=3. (**G-I**) Montage (**G**), kymograph (**H**) and plots (**I**) for a cell in the condition $C_o$=0, $\Delta C$=0 (**C**). Vertical scale for montages (**A, D, G**): 10 μm. Vertical scalebar for kymographs (**B, E, H**): 15 μm. Horizontal scalebar for kymographs (**B, E, H**): 100 seconds. Vertical dashed were added to both kymographs and time plots to represent the time at which the cell was determined to have de-polarized.

Figure 2: **Cells in uniform, non-zero concentrations exhibit a directional bias.** (**A**) Histograms of instantaneous cell polarizations (PH-Akt) for cells in uniform concentrations of 0 nM (yellow) and 10 nM fMLP (blue). For the histograms shown all polarizations prior to the first depolarization of a cell were removed as described in the methods. Arrows designate the mean polarization. (**B**) Mean values for histograms of instantaneous polarizations. (**C**) Skewness of histograms of instantaneous polarizations (see SI). (**D**) Statistics of re-polarization direction. Green represents the percentage of events for which a cell re-polarized in the **same** direction as prior to depolarization. Red represents the percentage of events for which a cell **switched** direction.

Figure 3: **Directional bias persists after removal of chemokine.** (**A**) Calculated plot of concentration as a function of time in the microchannel (wash @ t=0 sec, reintroduction @ t=120 sec). Solid lines represent the decay due to diffusion for a distance of 50 μm (black), 100 μm (red, slow decay) and 10 μm (red, fast decay) from the end of the channel. (**B**, **C**) Kymographs representing a cell re-polarizing in the same direction (**B**) and in the opposite direction (**C**). Red arrows mark the time when chemokine was removed (down) and reintroduced (up). Vertical scalebar: 15 μm. Horizontal: 100 seconds. (**D**) Re-polarization direction statistics for cells exposed to the dynamic environment. Chemokine removal for 2 or 10 minutes. Re-polarization by introducing chemokine only at the previous back of the cell ("Forced"). Spontaneously polarization in the absence of chemokine are also shown.

Figure 4: **Theoretical model of two-layer polarization reproduces directional bias.** (**A**) Model potential wells for a cell in a uniform low $C_o$ (i, $\alpha<0$), a uniform high $C_o$ (ii, $\alpha>0$) and $\Delta C>0$ (iii, $\alpha>0$). (**B**) Simulated cells in the conditions in **A**: (i) cells fluctuate about the unpolarized state p=0, (ii) cells tend to be in the polarized state $p=\pm 1$ and can switch direction. (iii) cells remain persistently polarized. (**C**) Directional re-polarization statistics for simulated cells for different cases of $C_o$ and $\Delta C$, including no coupling to $p_c$. (**D**) Simulations of the dynamic experiments exhibiting memory, where $C(t)>0$ (plotted in red as a function of time), then $C(t)=0$ (and cells depolarize), and then $C(t)>0$ again , whereupon cells re-polarize mostly in the original direction.

Figure 5: **Identification of long-lived cytoskeletal polarization.** (**A**) Representative kymograph MLC-mApple in a cell exposed to the dynamic environment described in Figure 3A. (**B**) Average relaxation curves for MLC-mApple and PH-Akt-GFP polarization. (**C**, **D**) Kymograph and average relaxation curves for moesin-mApple. (**E**) Directional re-polarization statistics for cells exposed to the dynamic environment (Figure 3) with drugs introduced upon chemokine removal and washed out upon chemokine reintroduction. (**F**, **G**) Kymographs of PH-Akt-GFP (**F**) and moesin-mApple (**G**) for a cell dynamically exposed to the ROCK inhibitor Y27632. Note the prolonged polarization of moesin in (**G**) compared to (**C**). (**H**, **I**) Average relaxation curves of moesin-mApple polarization for single drugs (**H**) and their combination (**I**). Decay plots represents the average value (solid) and standard deviation (dashed). Red arrows mark the time when chemokine was removed (down) and reintroduced (up). Vertical scalebar: 15 μm. Horizontal scalebar: 100 seconds.

Figure 6: **Microtubule disruption alters moesin polarization and disrupts memory**. (**A**) Directional repolarization statistics for cells exposed to colcemid alone or colcemid and Y27632 (**B**) Average relaxation curves of moesin-mApple for untreated cells, cells exposed to colcemid and cells exposed to both colcemid and Y27632. Solid lines represent the average value across the population, dashed lines represent one standard deviation.

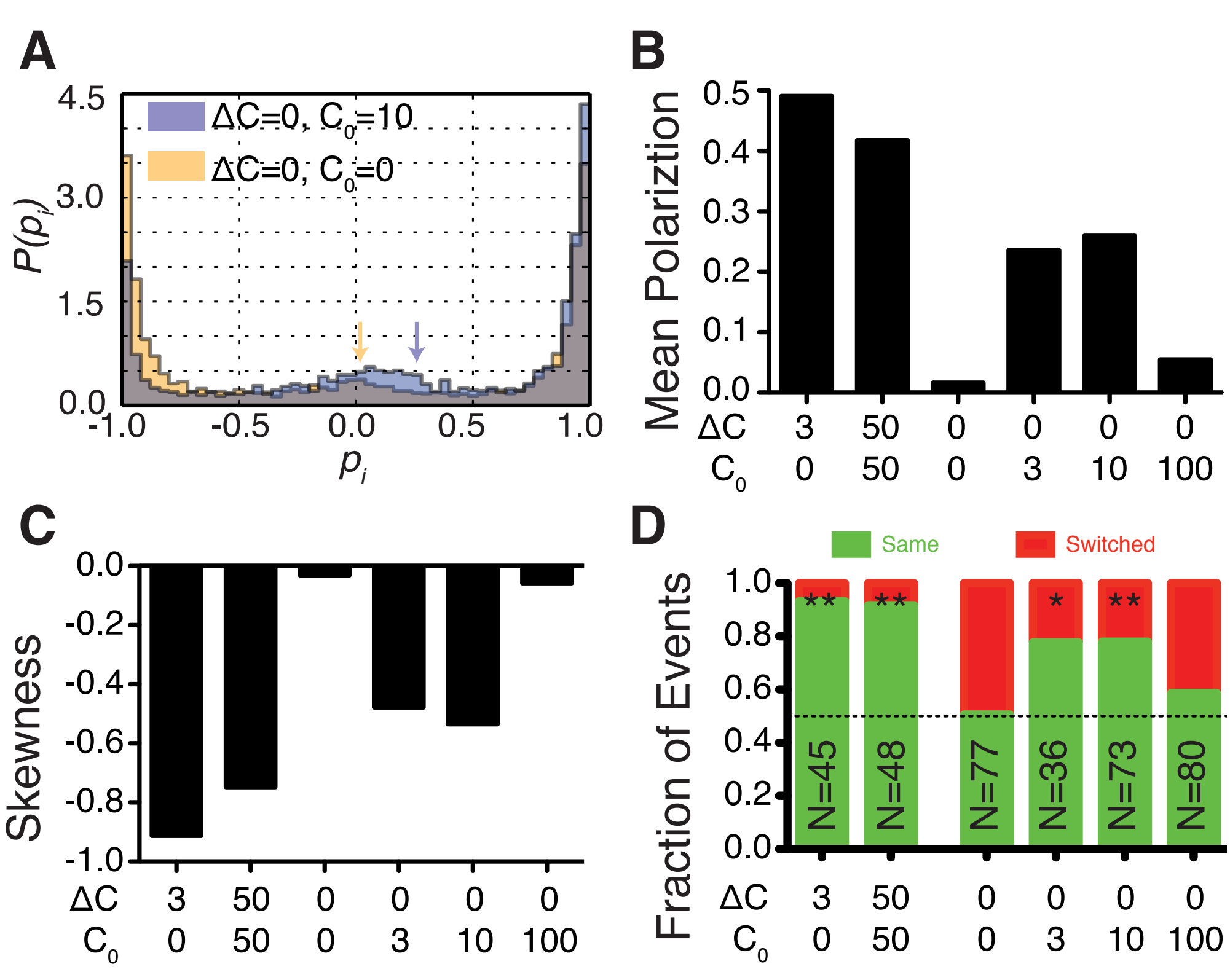
A
4.5
3.0
1.5
0.0
P(p_i)
ΔC=0, C_0=10
ΔC=0, C_0=0
-1.0
-0.5
0.0
0.5
1.0
p_i
B
Mean Polariztion
0.5
0.4
0.3
0.2
0.1
0.0
ΔC 3 50 0 0 0 0
C_0 0 50 0 3 10 100
C
Skewness
0.0
-0.2
-0.4
-0.6
-0.8
-1.0
ΔC 3 50 0 0 0 0
C_0 0 50 0 3 10 100
D
Same
Switched
Fraction of Events
1.0
0.8
0.6
0.4
0.2
0.0
**
**
*
**
N=45
N=48
N=77
N=36
N=73
N=80
ΔC 3 50 0 0 0 0
C_0 0 50 0 3 10 100

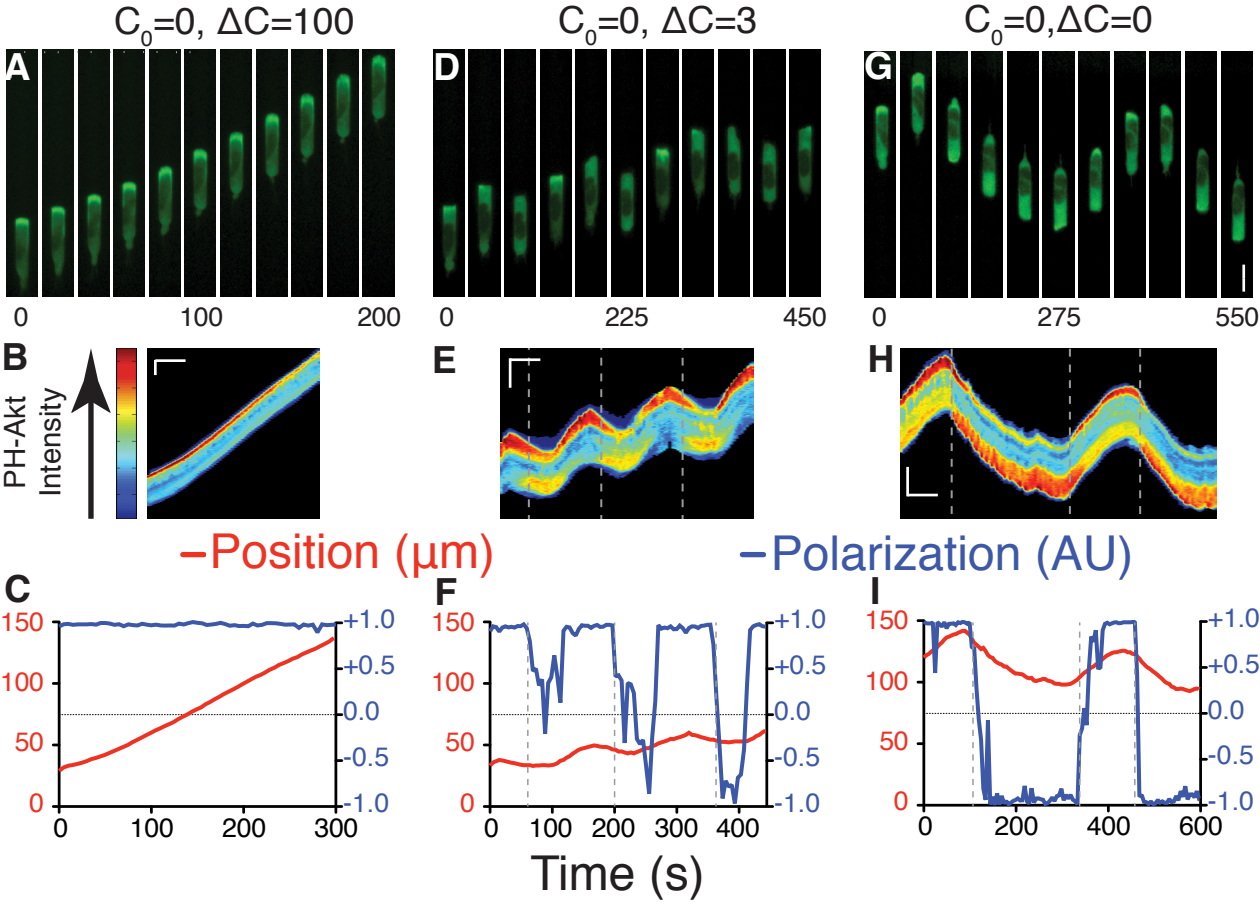
C0=0, ΔC=100
C0=0, ΔC=3
C0=0,ΔC=0
A
D
G
0
100
200
0
225
450
0
275
550
B
E
H
PH-Akt Intensity
Position (μm)
Polarization (AU)
C
F
I
150
100
50
0
+1.0
+0.5
0.0
-0.5
-1.0
0
100
200
300
400
600
Time (s)

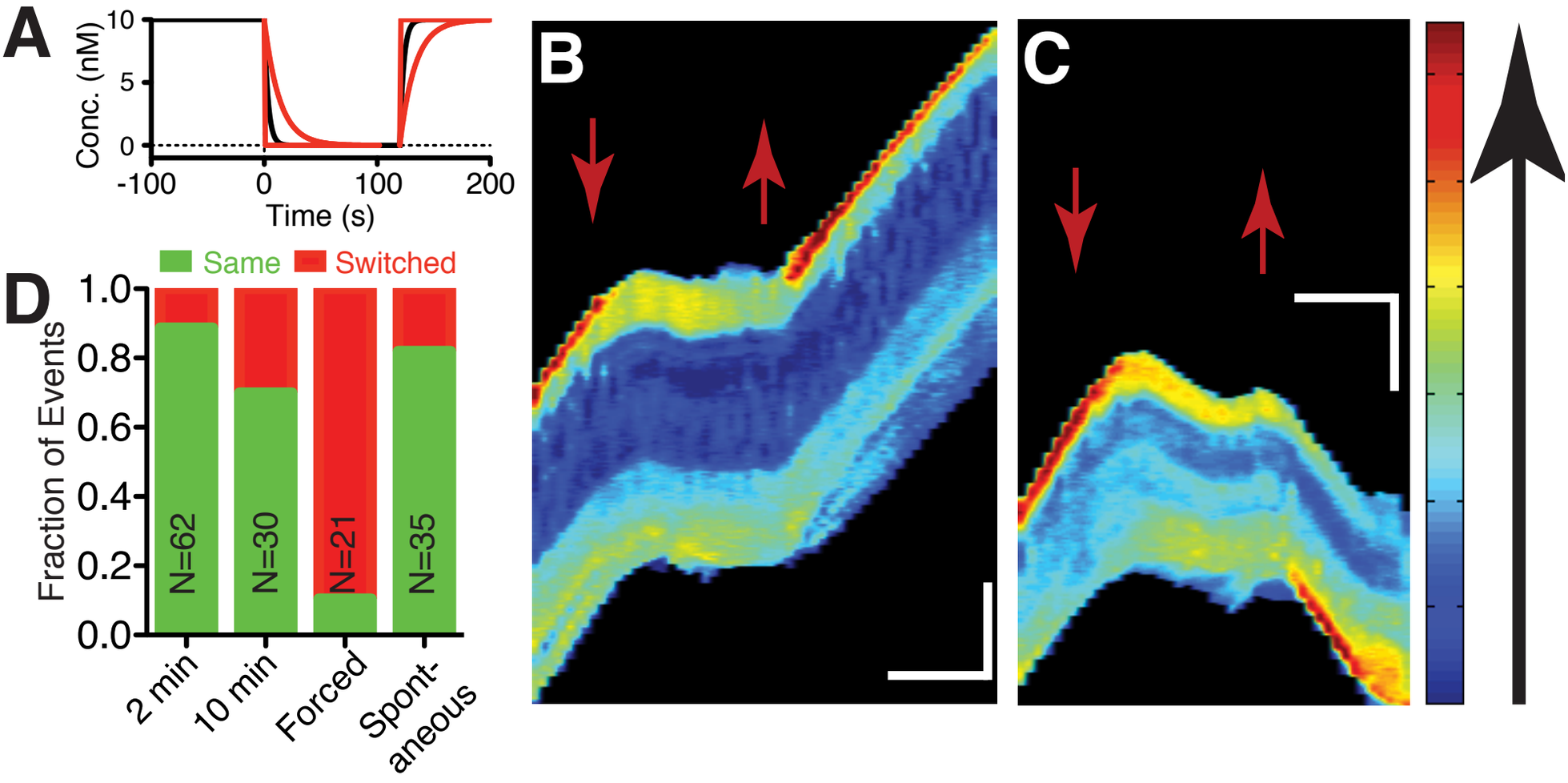
A
Conc. (nM)
10
5
0
-100
0
100
200
Time (s)
B
C
D
Same
Switched
Fraction of Events
1.0
0.8
0.6
0.4
0.2
0.0
N=62
N=30
N=21
N=35
2 min
10 min
Forced
Spont-
aneous

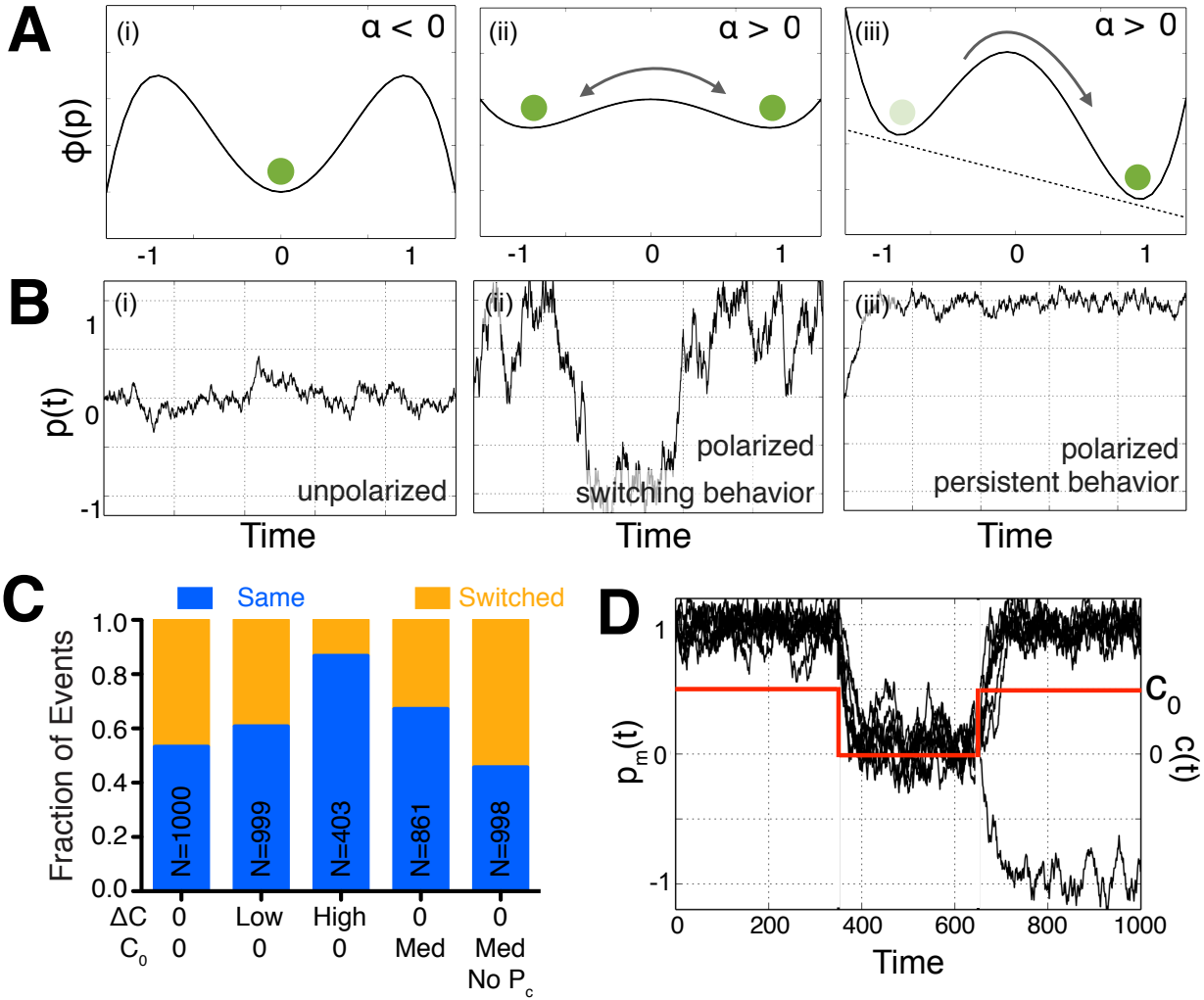
A
(i)
α < 0
(ii)
α > 0
(iii)
α > 0
ϕ(p)
-1
0
1
B
(i)
(ii)
(iii)
p(t)
1
0
-1
unpolarized
polarized
switching behavior
polarized
persistent behavior
Time
C
Same
Switched
Fraction of Events
1.0
0.8
0.6
0.4
0.2
0.0
N=1000
N=999
N=403
N=861
N=998
ΔC
C0
0
0
Low
0
High
0
0
Med
0
Med
No Pc
D
pm(t)
c(t)
C0
1
0
-1
0
200
400
600
800
1000
Time

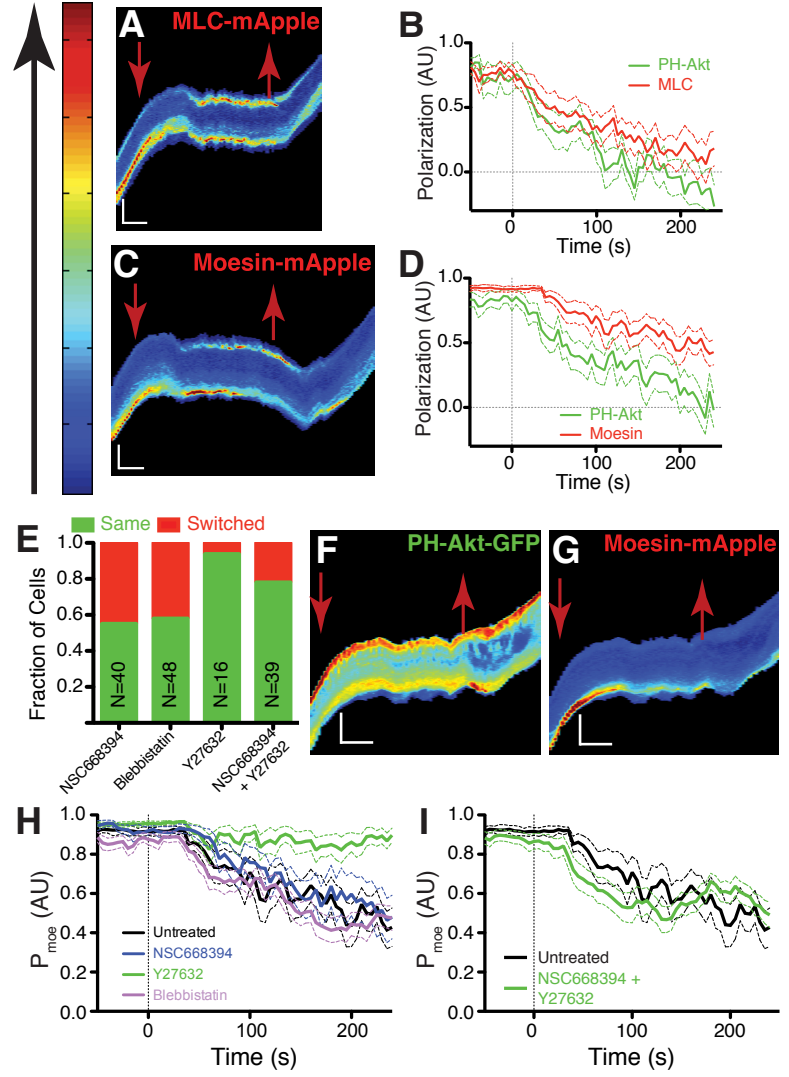
A
MLC-mApple
B
PH-Akt
MLC
Polarization (AU)
Time (s)
C
Moesin-mApple
D
PH-Akt
Moesin
Polarization (AU)
Time (s)
E
Same
Switched
Fraction of Cells
N=40
N=48
N=16
N=39
NSC668394
Blebbistatin
Y27632
NSC668394 + Y27632
F
PH-Akt-GFP
G
Moesin-mApple
H
Untreated
NSC668394
Y27632
Blebbistatin
P moe (AU)
Time (s)
I
Untreated
NSC668394 + Y27632
P moe (AU)
Time (s)

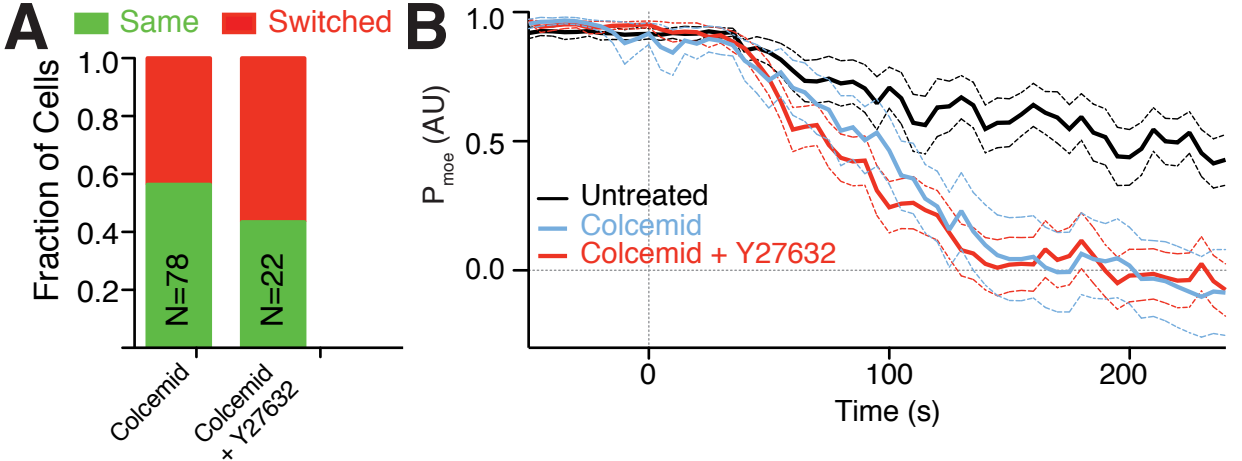
A
Same
Switched
Fraction of Cells
1.0
0.8
0.6
0.4
0.2
N=78
N=22
Colcemid
Colcemid + Y27632
B
1.0
0.5
0.0
P moe (AU)
Untreated
Colcemid
Colcemid + Y27632
0
100
200
Time (s)

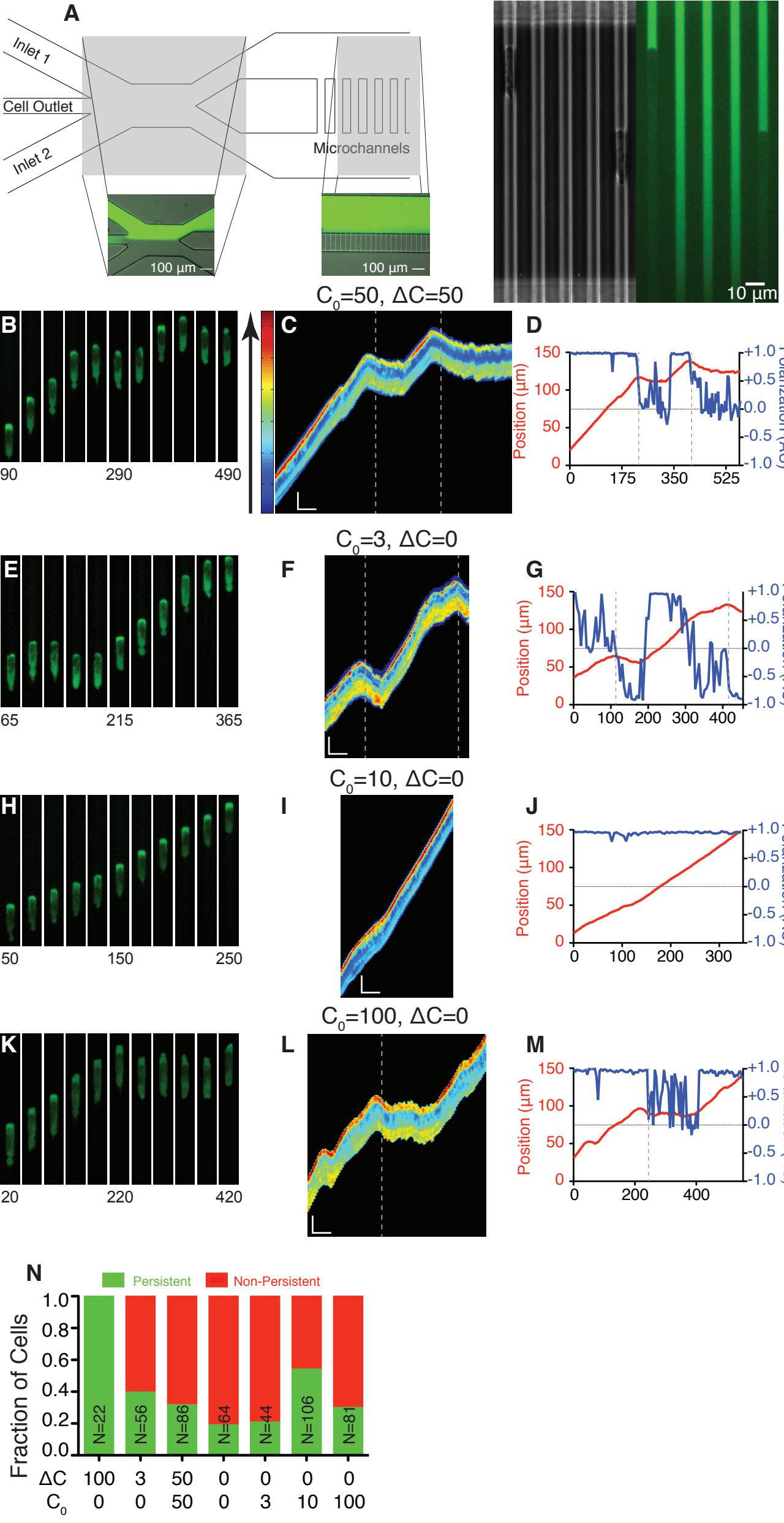
A
Inlet 1
Cell Outlet
Inlet 2
Microchannels
100 µm
100 µm
10 µm
C0=50, ΔC=50
B
C
D
90
290
490
Position (µm)
Polarization (AU)
C0=3, ΔC=0
E
F
G
65
215
365
C0=10, ΔC=0
H
I
J
50
150
250
C0=100, ΔC=0
K
L
M
20
220
420
N
Persistent
Non-Persistent
Fraction of Cells
N=22
N=56
N=86
N=64
N=44
N=106
N=81
ΔC 100 3 50 0 0 0 0
C0 0 0 50 0 3 10 100

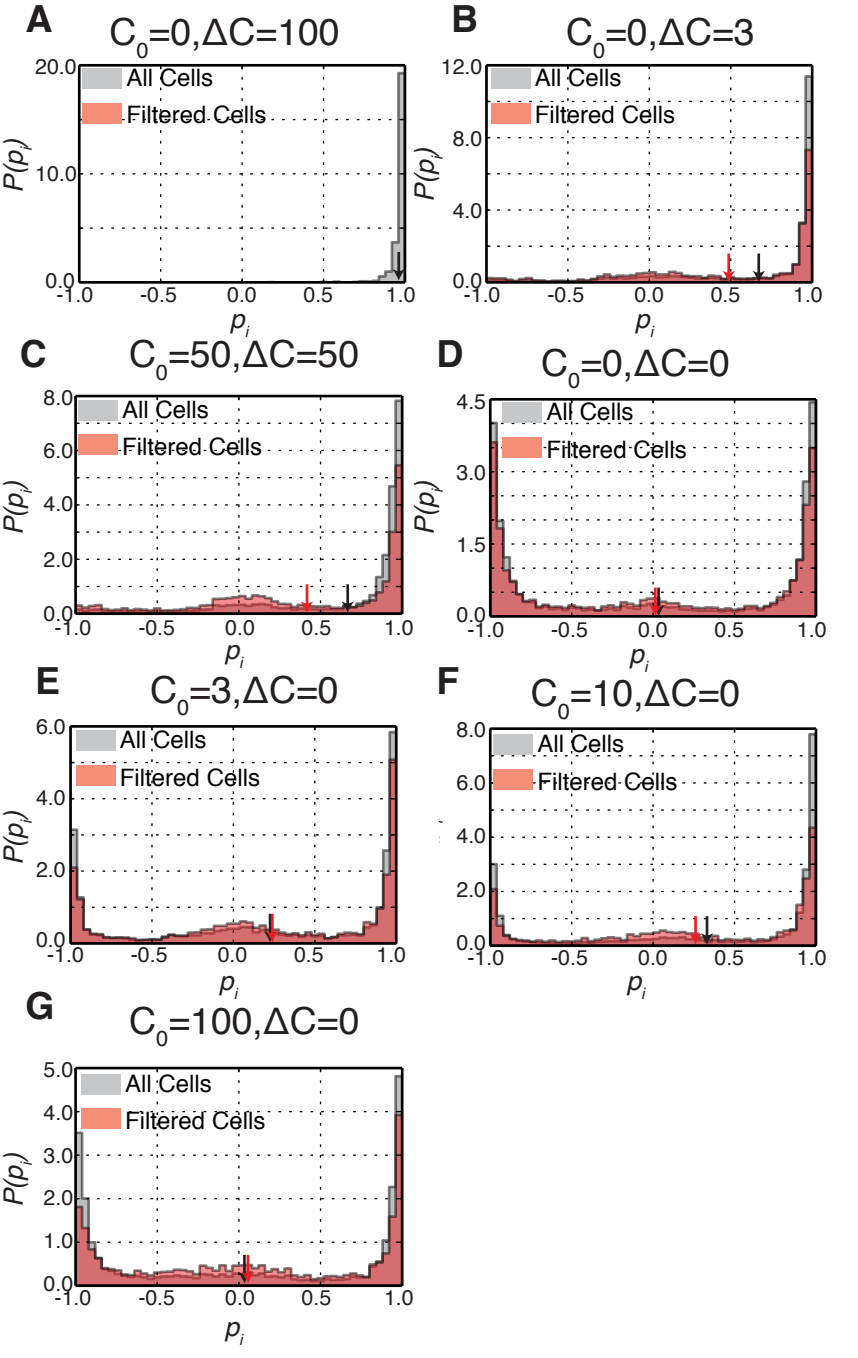
A
C0=0,ΔC=100
B
C0=0,ΔC=3
C
C0=50,ΔC=50
D
C0=0,ΔC=0
E
C0=3,ΔC=0
F
C0=10,ΔC=0
G
C0=100,ΔC=0
All Cells
Filtered Cells
P(pi)
pi

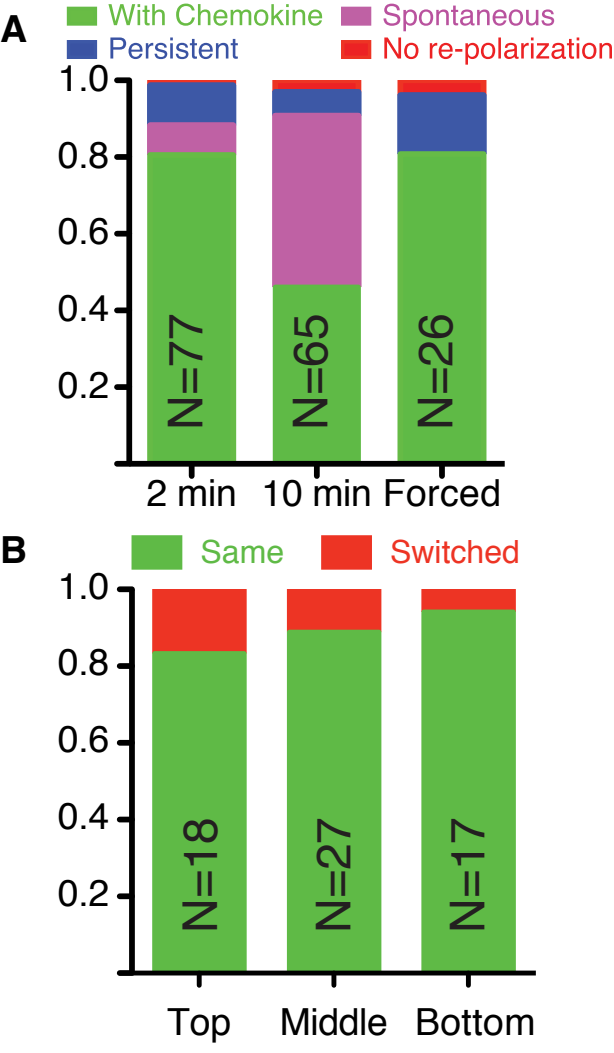
A
With Chemokine
Spontaneous
Persistent
No re-polarization
1.0
0.8
0.6
0.4
0.2
N=77
N=65
N=26
2 min
10 min
Forced
B
Same
Switched
1.0
0.8
0.6
0.4
0.2
N=18
N=27
N=17
Top
Middle
Bottom

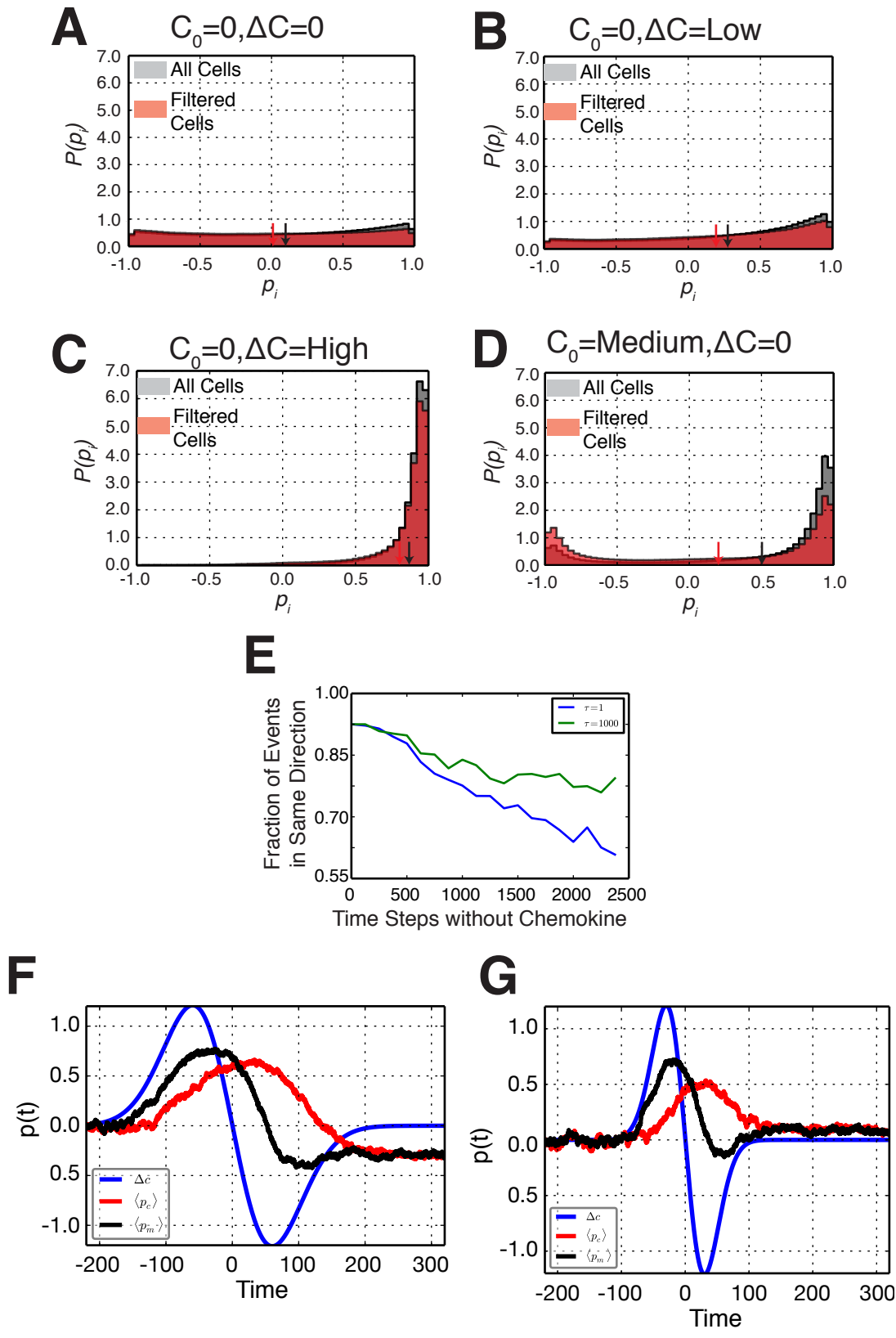
A
$C_0$=0,ΔC=0
All Cells
Filtered Cells
$P(p_i)$
$p_i$
B
$C_0$=0,ΔC=Low
C
$C_0$=0,ΔC=High
D
$C_0$=Medium,ΔC=0
E
Fraction of Events in Same Direction
Time Steps without Chemokine
$\tau$=1
$\tau$=1000
F
G
p(t)
Time
$\Delta c$
$\langle p_c \rangle$
$\langle p_m \rangle$

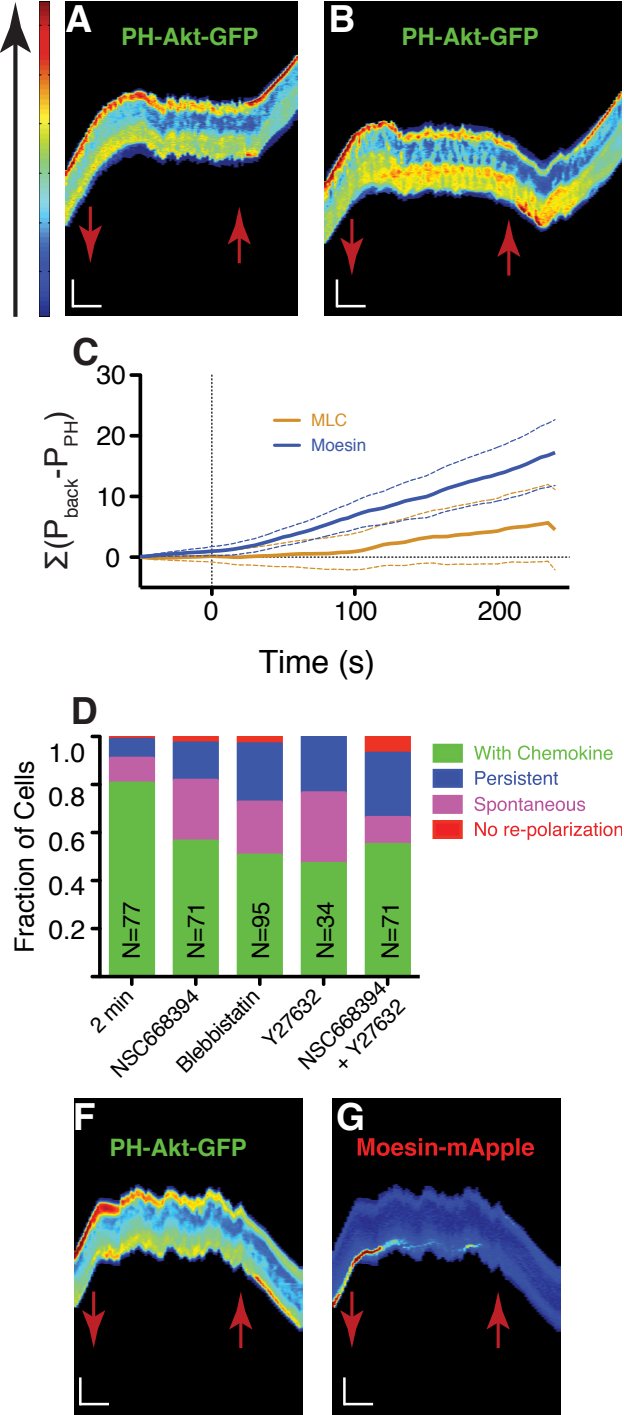
A
PH-Akt-GFP
B
PH-Akt-GFP
C
30
20
10
0
$\Sigma(P_{back}-P_{PH})$
MLC
Moesin
0
100
200
Time (s)
D
Fraction of Cells
1.0
0.8
0.6
0.4
0.2
N=77
N=71
N=95
N=34
N=71
With Chemokine
Persistent
Spontaneous
No re-polarization
2 min
NSC668394
Blebbistatin
Y27632
NSC668394 + Y27632
F
PH-Akt-GFP
G
Moesin-mApple

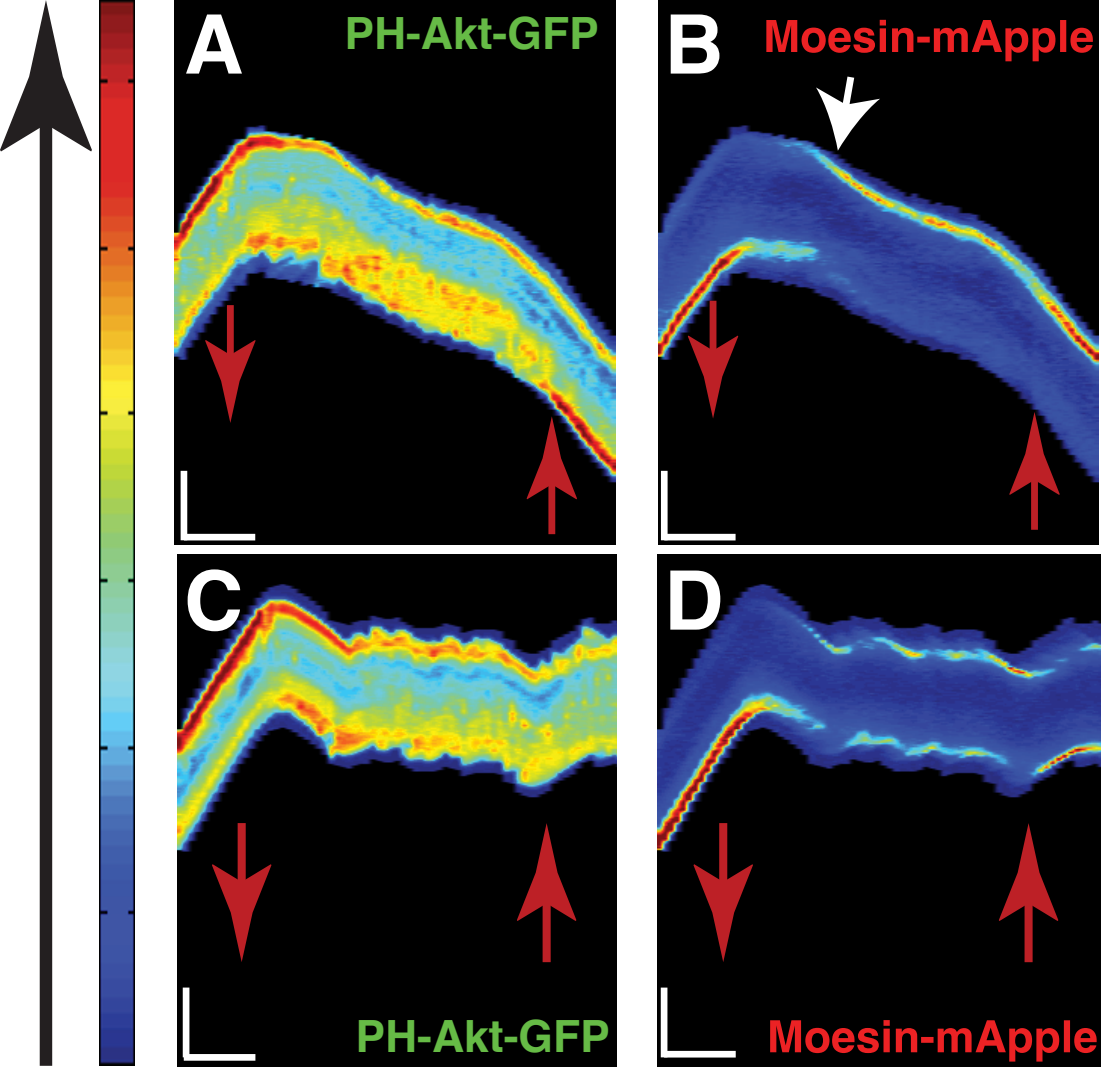
A
PH-Akt-GFP
B
Moesin-mApple
C
PH-Akt-GFP
D
Moesin-mApple

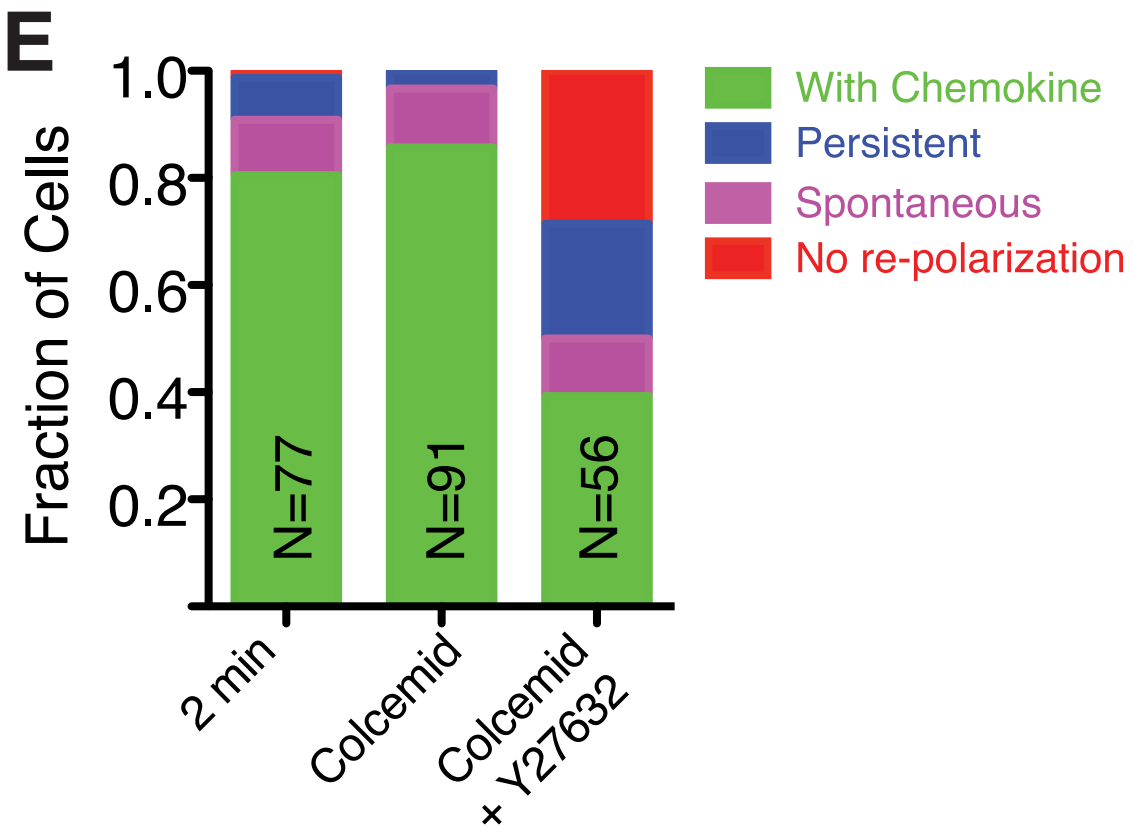
E
Fraction of Cells
1.0
0.8
0.6
0.4
0.2
N=77
N=91
N=56
2 min
Colcemid
Colcemid + Y27632
With Chemokine
Persistent
Spontaneous
No re-polarization

## Experimental Procedures

### Cell Culture and Stable Line Production:

HL-60 cultures were maintained in RPMI 1640 (Invitrogen, 11875119) media supplemented with 20% FBS (Invitrogen, 26104), 1% Penstrep (Cellgro, 30-002-CI), and 25 mM sterile filtered HEPES (Fisher Scientific, BP310), and were passaged every 2-3 days. Cells were differentiated in complete media supplemented with DMSO to a final concentration of 1.3%. Cells differentiated for at least 5 days and not more than 7 days were used for experiments.

Cell lines stably expressing PH-Akt-GFP were generated via retroviral infection, as described previously [5]. Briefly, Plat-GP cells (Cell Biolabs, San Diego, CA) were used to produce retrovirus by co-transfection with a pBABE packaging vector (pBABEblast, pJag98 containing the cDNA for 3xPH-Akt-GFP (cDNA obtained from Lew Cantley, Harvard Medical School) and VSV-G, using Fugene 6 (Roche, Germany). Lentiviral particles were generated as described previously [5], with the exception that 293T cells were used and a pCDH packaging vector (Systems Biosciences) was co-transfected with the helper plasmids psPAX2 (Addgene #12260) and pMD2.G (Addgene #12259). The viral supernatants (both lenti and retro) were collected after 48-72 hours and filtered using a 0.45 micron syringe filter.

Polybrene was added to the supernatant at a final concentration of 16 micrograms/mL. Cells were suspended in one well of a 6-well plate at a concentration of $10^6$/mL in a volume of 2 mL. To this suspension was added 5 mL of viral supernatant and the cells were spun at 1000xg for 90 minutes in a swinging bucket rotor. Cells were then incubated for 5 hours at 37 C. Following this incubation, cells were pelleted and resuspended into 2 mL fresh media. The next day, 2 mL of fresh media was added to the cells. The next day, cells were placed under selection in 1 micrograms/mL blasticidin. Once a stable pool of blasticidin resistant cells was obtained, the cells were then sorted for GFP expression (HMS/Systems Biology Flow Cytometry Facility).

### Microfluidic Device Fabrication:

Microfluidic devices were generated as described previously [5, 8]. High-resolution film (Fineline Imaging, Colorado Springs, CO) or chrome (Advanced Reproductions Corp, Andover, MA; Front-Range Photomasks, Colorado Springs, CO) masks were used to generate photoresist masters. SU-8 (Microchem, Newton, MA) was spun onto silicon wafers at a rate according to the feature height desired. The photoresist was then exposed to UV light using a mask aligner (Neutronix Quintel, Morgan Hill, CA). Unexposed SU-8 was developed away. PDMS was then either spun (for membranes) or poured onto the wafers, cured overnight at 70 C. The top layer of the devices was then cut out, access holes were punched for pneumatic valve control using a 0.75 mm diameter punch, and the devices were then bonded to the spun membrane using oxygen plasma. These devices were again cut out and

additional fluid access holes were punched and the devices were then bonded to either 1x3 glass slides (Fisher Scientific, Pittsburgh, PA), or 45x50 mm No. 1.5 coverslips (Fisher Scientific, Pittsburgh, PA).

**Microfluidic Device Operation:**

Tygon tubing (Greene Rubber Company, part no., 2007900S-54HL) and 30 gauge blunt syringe needles (Brico Medical Supplies, BN2505) were used to connect syringes to the microfluidic devices. The outer diameter of the tygon tubing (0.03 in) is slightly larger than the diameter of the hole punched, so when the tubing was inserted into the hole, a seal was created. Each of the pneumatic valve control chambers was connected to a 1 mL syringe. To close the valves, the syringe was compressed from a volume of 0.2 mL to approximately 0.05 mL. To open the valves, the syringes were pulled open from a volume of 0.2 mL to the maximum volume of the syringe.

Fibronectin was adsorbed onto the channel walls by filling the device with a solution containing 50 micrograms/mL fibronectin (Sigma-Aldrich, F0895) in 50 mM Tris-HCl. Any air bubbles present were removed by pressurizing the device. The solution was incubated in the device for 1 hour at room temperature and then rinsed out with HBSS supplemented with 25 mM HEPES and 0.2% human serum albumin.

Each inlet was connected to a syringe, with the plunger removed. One syringe contained a solution of HBSS, while the other contained a solution of HBSS with fMLP. Fluorescein was added to the syringe containing fMLP to visualize the interface of the two inlet streams for balancing the stream pressures. To reduce the introduction of air bubbles while loading cells, a drop of HBSS was placed onto the cell inlet hole prior to removing the priming tubing.

To load cells into the device, 2-3 mL of differentiated cells were pelleted and 30 $\mu$L of the cell pellet was taken and placed into a blunt needle with a short section of tubing. The cells were then pushed through the tubing by applying pressure to the top of the needle with a finger, until a small drop appeared at the end of the tubing in order to provide a liquid-liquid interface while inserting the tubing to prevent the introduction of air bubbles. The cells were then pushed into the device by applying pressure with a finger and the on-chip valves were manipulated to control whether cells were loaded on only side of the microchannels or on both sides.

When inhibitors were used (10 $\mu$M colcemid (EMD Millipore), 50 μM NSC688394 (EMD Millipore), 20 $\mu$M Y-27632 (Tocris) or 50 $\mu$M blebbistatin (Abcam)), they were added to the 0 nM reservoir. For the experiments in which inhibitors were tested, either 10 $\mu$M colcemid (EMD Millipore) or 50 $\mu$M NSC688394 (EMD Millipore) was added to the 0 nM reservoir.

**Image Acquisition and Analysis:**

Cells were imaged on either a Nikon TE2000 microscope (Nikon) or a Nikon Eclipse Ti (Nikon) with a 40x Ph3 Plan Apo (Nikon) objective. The microscopes were controlled with the Volocity software package (Perkin Elmer, Waltham, MA) or Nikon Elements (Nikon), respectively. Images were acquired at a frame rate of 1 frame every 5s, in both the GFP and bright-field channels.

For each cell, the central 30% of the channel was extracted, and the image was averaged over the width of the channel for each time point, generating a one-dimensional intensity profile. The edge of the cell was then determined, at each time point, by applying a nonlinear filter [36] and an adaptive threshold was implemented with a constraint on cell length determined from the previous frame to find the edges of the cell. All images were analyzed with in-house Matlab (MathWorks Inc.) algorithms.

The polarization was determined using a clustering method similar to that described by Ku et al. [11]. First, the locations of the top 5% of pixels, by intensity, were found. The average pair-wise distance between these pixel locations was then calculated. Next, the theoretical minimum average pair-wise distance was calculated by generating a disc of the same area as the top 5% pixels identified and the theoretical maximum average pair-wise distance was calculated by distributing an equal number of pixels through a region of the same size as the cell. The measured average pair-wise distance was then subtracted from the maximum theoretical average and the result was divided by the difference of the theoretical minimum from the theoretical maximum, giving a value ranging between 0 and 1. The orientation of the polarization was then determined by comparing the center of mass of the 5% brightest pixels and the center of the cell. This process was performed for each time step, and the resulting polarization trajectory was scaled by the initial orientation such that each cell starts with a positive polarization.

Skewness of polarization histograms was calculated as the third central moment divided by the standard deviation cubed.

**Model Description:**

Here we complement the description of polarization dynamics embodied in Eq. (1) by accounting for the dynamics and constraints on the membrane polarization gain $\alpha_m$. The fraction of bound receptors n is related to the chemokine concentration c and the dissociation constant $K_d$ through $n= c/(c+K_d)$. The gain associated with the membrane polarization $\alpha_m$ is a function of the rate of binding events $n_{on} = k_+c(1-n) = nk_+K_d$ , where $k_+$ is the rate of association of a chemokine ligand to a receptor. We take $n_{on}$ to be the average of n on both sides $n_{on} = k_+K_d(n_L+n_R)/2$. $\alpha_m$ increases with $n_{on}$ (assumed here to grow linearly for simplicity), effectively lowering the ratio to the noise, i.e. the stronger the signal (the higher the fraction of bound receptors) the lower the noise. We also assume a minimal value for $\alpha_m$ so that:

Eq. (S1) $$\alpha_m(n_{on}) \sim n_{on}^{min}, \quad n_{on} < n_{on}^{min}$$

$$\alpha_m(n_{on}) \sim n_{on}, \qquad n_{on} > n_{on}^{min}$$

As mentioned in *Results*, the gain is itself is stochastically driven by a noise term $\eta_\alpha$, so that

Eq. (S2) $$d\alpha_m/dt = \eta_\alpha ,$$

but restricted to the initial values set in Eq. (S1). This allows $\alpha_m$ to randomly switch signs and therefore allows the cell to de-polarize and re-polarize spontaneously, as also seen experimentally. The gain associated with the polarization of the cytoskeleton is slaved to $\alpha_m$ but is also a function $p^*_m$ the history of the membrane polarization: $\alpha_c = \alpha_m|p^*_m|$. A persistent (switching) membrane polarization is reflected in a maximal (low) value of its history $p^*_m$, and hence lowering (raising) the sensitivity of the cytoskeleton polarization. This reasoning hinges again on the notion that the cytoskeleton reacts to the membrane polarization on a longer time scale. We also point that while solving (Eqs. 1, S1, S2) we also enforce reflecting boundary conditions have been set for $p_m$ and $p_c$ at the extreme values+1 and -1, since values beyond this range are not defined, and have no physical meaning.

The parameters used in our simulations are: $\eta$=5.0, $\eta_\alpha$=8.0, $k_+K_d$=4.0, $n_{on}^{min}$=0.1, $\tau$=100.

The value $n_{on}^{min}$=0.1 was chosen arbitrarily as a small number in the range [0,1]. The value for $k_+K_d$ was chosen to be double the distance between the two wells of the double-well potential (i.e. 2), since this parameter sets the depth of the wells. The noise $\eta$, i.e. the standard deviation of the Gaussian noise, was taken to be slightly larger than the depth of the wells, therefore allowing $p^*_m$ to hop between the two wells, but allowing some residence time within each well. This value can be associated with the experimental residence time in each polarization state when there is no gradient. Lastly the value for the noise driving $\alpha_m$ the gain of the membrane polarization $\eta_\alpha$ is what sets the rate of spontaneous polarization or depolarization. Considering the distribution of time spent in different polarizations, Fig. (2A), we can discern three peaks: p=1 and p=-1 are roughly equal in magnitude, and a smaller peak at p=0. The ratio of polarized/unpolarized peaks is set by $\eta_\alpha$. In our simulations it was chosen so as to best reproduce the experimentally reported ratio. Furthermore it is important to note that if this parameter set to be too low, the gain does not change sign often enough, not allowing the polarization to change direction often enough, i.e. the dynamics may seem persistent within some timeframe. This finding calls our attention to the notion that biological systems may be poised at criticality, allowing versatility without paying in robustness. Lastly, in the simulations we considered the same cases of concentrations as in the experiments, translating them to $n_{on}$ and $\Delta n$ through the relations $n_{on} = k_+K_d(n_L+n_R)/2$ and $\Delta n = k_+K_d(n_L-n_R)/2$, where $n_L=c_L/(c_L+K_d)$ and $n_R=c_R/(c_R+K_d)$, and $K_d$=10 (a typical value [12], where c and Kd are experessed in nM). We also note $K_d$=10 nM yields $k_+$=0.4 1/s nM, also typical. The relevant values for the different cases of concentrations, expressed as fractions of bound receptors are: C0-0: $n_{on}$=0 $\Delta n$=0, C0-3: $n_{on}$=0.12 $\Delta n$=0.23, C50-100: $n_{on}$=0.87 $\Delta n$=0.08, C0-100: $n_{on}$=0.46 $\Delta n$=0.91, C10-10: $n_{on}$=0.5 $\Delta n$=0.

**Supplemental Figure Legends**

Figure S1: **Device design and cellular response to static chemical environments.** (**A**) Diagram of device geometry. Two inlet channels are used to introduce chemokine solutions into the device. The cell outlet channel is used when cells are introduced into the device from the outlet, downstream of the microchannel region. Insets demonstrate the positioning of the interface between the two inlet flows to balance pressure and maintain concentration difference across the microchannels. Fluorescein dye was used to visualize the separate streams. Inset shows a cell occluding a microchannel, resulting in build-up of chemokine in front, as well as a microchannel without a cell resulting in a gradient of dye along the length of the channel. (**B**, **E**, **H**, **K**) Montages of cells expressing PH-Akt-GFP in the conditions $C_0$=50 $\Delta C$=50 (**B**), $C_0$=3 $\Delta C$=0 (**E**), $C_0$=10 $\Delta C$=0 (**H**) and $C_0$=100 $\Delta C$=0 (**K**). (**C**, **F**, **I**, **L**) Kymographs of cells shown in montages. Kymographs are false-colored according to the color bar shown on the left to better visualize differences in PH-Akt intensity. Vertical scalebar: 15 μm. Horizontal scalebar: 100 seconds. (**D**, **G**, **J**, **M**) Plots of cell centroid and PH-Akt polarization for corresponding montages. (**N**) Fraction of persistently polarized (green) and not persistently polarized (red) in the static conditions tested. Vertical dashed were added to both kymographs and time plots to represent the time at which the cell was determined to have de-polarized.

Figure S2: **Histograms of instantaneous cell polarizations.** Given that the vast majority of cells were polarized at the start of the observation period we plotted the histogram of the entire trajectory (grey histogram) as well as the trajectory after the first depolarization event (red histogram) for all static conditions. While there was a shift in the first-depolarization histogram, even small chemotactic differences resulted in a strong bias toward the original direction. $C_0$=0 $\Delta C$=100 (**A**), $C_0$=0 $\Delta C$=3 (**B**), $C_0$=50 $\Delta C$=50 (**C**), $C_0$=0 $\Delta C$=0 (**D**), $C_0$=3 $\Delta C$=0 (**E**), $C_0$=10 $\Delta C$=0 (**F**), $C_0$=100 $\Delta C$=0 (**G**). Red and black arrows demonstrate the mean values for the two distributions in each condition.

Figure S3: **Cellular responses to dynamics change in chemokine**. (**A**) Percentage of cells that did not depolarize upon removal of chemokine (Persistent) or depolarized upon removal of chemokine and either repolarized upon reintroduction of chemokine (Normal), re-polarized prior to reintroduction of chemokine (Spontaneous) or did not depolarize (No re-polarization). (**B**) Cells were separated by whether they were in the bottom, middle or top third of the microchannel, relative to the end at which they entered. As can be seen, the directional memory of the cells was not dependent on the position of the cell in the microchannel.

Figure S4: **Histograms of simulated cell polarizations**. Histograms of simulated cellular polarizations including all polarization measurements (grey) and only those that occurred following the first depolarization of a cell (red) for the conditions $C_0$=0 $\Delta C$=0 (**A**), $C_0$=0 $\Delta C$=Low (**B**), $C_0$=0 $\Delta C$=High (**C**), $C_0$=Medium $\Delta C$=0 (**D**). (**E**) Directional re-polarization statistics for simulated cells as a function of

the amount of time between removal and reintroduction of chemokine for two parameters of the timescale of the memory kernel: smaller timescale with $\tau$=1 in blue, and a larger timescale with $\tau$=1000 in green. The larger timescale exhibits longer memory compared to the smaller timescale, with a higher fraction of cells repolarizing in the same direction at any time. (**F**) For slow waves, where the timescale of the positive gradient $\tau_{\Delta n}$ = 200 is larger than the timescale of the memory kernel $\tau_{pc}$,=100, the polarization of the membrane switches directions as seen by the final negative p(t) at long times. (**G**) For faster waves, where $\tau_{\Delta n}$ = 100 is comparable to $\tau_{pc}$, the cell exhibits directional memory, and does not switch polarization directions as seen by the positive p(t) at long times. Details found in the main text.

Figure S5: **Identification of long-lived cytoskeletal polarization**. (**A**, **B**) Kymographs of PH-Akt-GFP localization for cells expressing either MLC-mApple (**A**) or moesin-mApple (**B**), shown in Figure 5 (**A**) and (**C**), respectively. Red arrows mark the time when chemokine was removed (down) and reintroduced (up). Vertical scalebar: 15 μm. Horizontal scalebar: 100 seconds. (**C**) Cumulative sum of the difference between either MLC or moesin polarization and PH-Akt polarization. (**D**) Responses of cells to removal and reintroduction of chemokine (as described in Figure S3) for the different drugs and drug combinations tested. (**E**, **F**) Kymographs of PH-Akt-GFP (**E**) and moesin-mApple (**F**) for a cell treated with moesin inhibitor NSC668394.

Figure S6: **Microtubule disruption alters relaxation dynamics of moesin polarization**. (**A**, **B**) Kymographs of PH-Akt-GFP (**A**) and moesin-mApple (**B**) for a cell dynamically exposed to the microtubule inhibitor colcemid. Red arrows mark the time when chemokine was removed (down) and reintroduced (up). Vertical scalebar: 15 μm. Horizontal scalebar: 100 seconds. (**C**, **D**) Kymograph of PH-Akt-GFP (**C**) and moesin-mApple for a cell exposed to the combination of colcemid and Y27632 (**D**). Red arrows mark the time when chemokine was removed (down) and reintroduced (up). Vertical scalebar: 15 μm. Horizontal scalebar: 100 seconds. (**E**) Responses of cell to removal and reintroduction of chemokine (as described in Figure S3) for treatment both with colcemid alone as well as drug combinations including colcemid.

**Supplementary Movie Legends**

Movie S1: Movie of cell shown in Figure 1A ($\Delta C$=100 $C_o$=0). Scalebar: 10 μm

Movie S2: Movie of cell shown in Figure 1D ($\Delta C$=3 $C_o$=0). Scalebar: 10 μm

Movie S3: Movie of cell shown in Figure 1G ($\Delta C$=0 $C_o$=0). Scalebar: 10 μm

Movie S4: Movie of cell shown in Figure S1B ($\Delta C$=50 $C_o$=50). Scalebar: 10 μm

Movie S5: Movie of cell shown in Figure S1E ($\Delta C$=0 $C_o$=3). Scalebar: 10 μm

Movie S6: Movie of cell shown in Figure S1H ($\Delta C$=0 $C_o$=10). Scalebar: 10 μm

Movie S7: Movie of cell shown in Figure S1K ($\Delta C$=0 $C_o$=100). Scalebar: 10 μm

Movie S8: Movie of cell shown in kymograph in Figure 3B, repolarizing in the same direction up reintroduction of chemokine. Chemokine was removed at t=0 and reintroduced at t=85. Scalebar: 10 μm.

Movie S9: Movie of cell shown in kymograph in Figure 3B, repolarizing in the opposite direction up reintroduction of chemokine. Chemokine was removed at t=0 and reintroduced at t=115. Scalebar: 10 μm.

Movie S10: Movie of cell shown in kymograph in Figure 5A, expressing PH-Akt-GFP (green) and MLC-mApple (red). Chemokine was removed at t=0 and reintroduced at t=300. Scalebar: 10 μm.

Movie S11: Movie of cell shown in kymograph in Figure 5C, expressing PH-Akt-GFP (green) and hsMoesin-mApple (red). Chemokine was removed at t=0 and reintroduced at t=320. Scalebar: 10 μm.

Movie S12: Movie of cell shown in kymograph in Figure 5F,G, expressing PH-Akt-GFP (green) and hsMoesin-mApple (red), and treated with the ROCK inhibitor Y27632. Chemokine was removed and drug introduced at t=0 and the chemokine was reintroduced and the drug removed at t=260. Scalebar: 10 μm.

Movie S13: Movie of cell shown in kymograph in Figure S5F,G, expressing PH-Akt-GFP (green) and hsMoesin-mApple (red), and treated with the ezrin inhibitor NSC668394. Chemokine was removed and drug introduced at t=0 and the chemokine was reintroduced and the drug removed at t=300. Scalebar: 10 μm.

Movie S14: Movie of cell shown in kymograph in Figure 5A,B, expressing PH-Akt-GFP (green) and hsMoesin-mApple (red), and treated with the microtubule depolymerizer colcemid. Chemokine was removed and drug introduced at t=0 and the chemokine was reintroduced and the drug removed at t=265. Scalebar: 10 μm.

Movie S15: Movie of cell shown in kymograph in Figure 5C,D, expressing PH-Akt-GFP (green) and hsMoesin-mApple (red), and treated with both colcemid and Y27632. Chemokine was removed and drug introduced at t=0 and the chemokine was reintroduced and the drug removed at t=250. Scalebar: 10 μm.

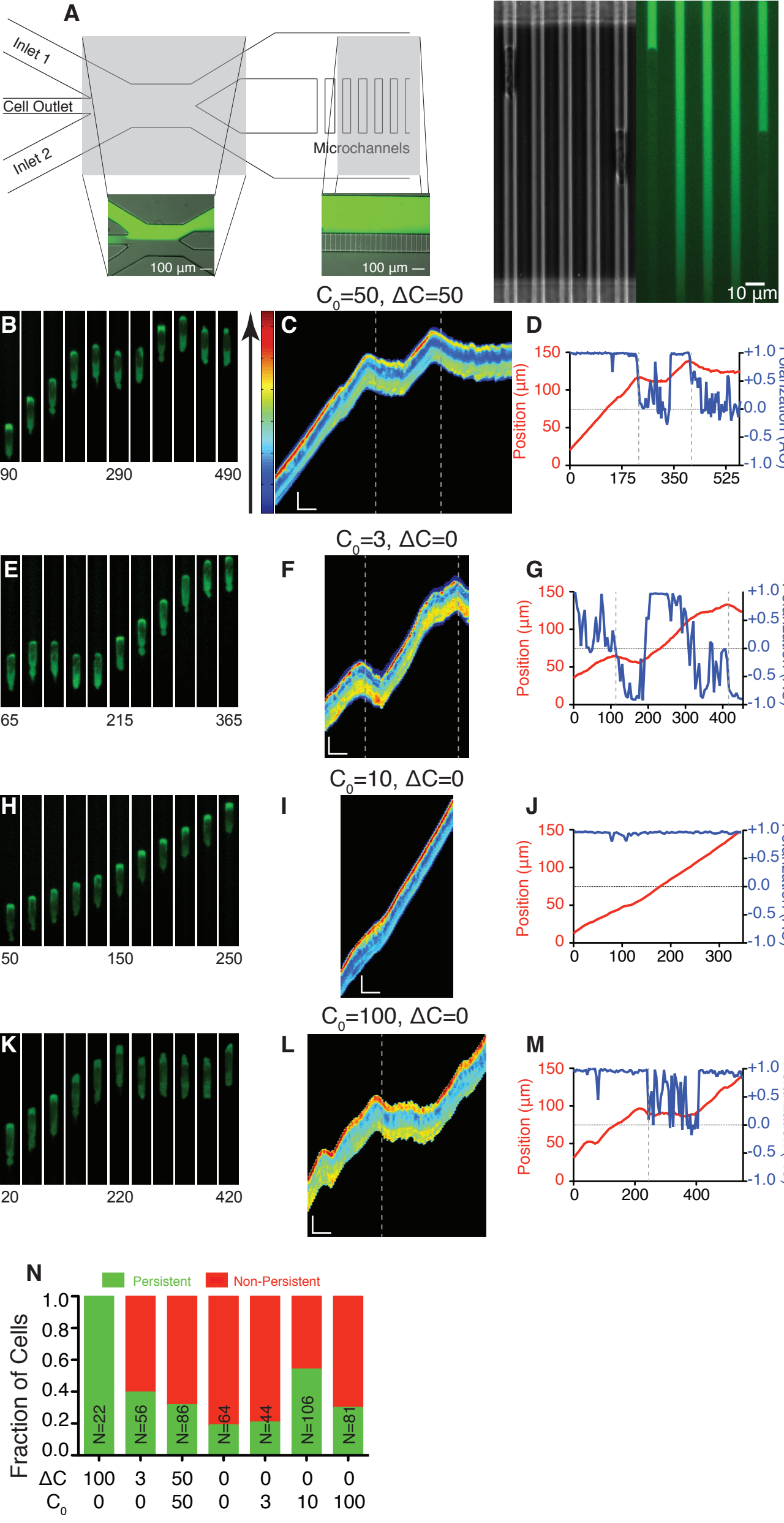
A
Inlet 1
Cell Outlet
Inlet 2
Microchannels
100 µm
100 µm
10 µm
C0=50, ΔC=50
B
C
D
90
290
490
Position (µm)
Polarization (AU)
C0=3, ΔC=0
E
F
G
65
215
365
C0=10, ΔC=0
H
I
J
50
150
250
C0=100, ΔC=0
K
L
M
20
220
420
N
Persistent
Non-Persistent
Fraction of Cells
N=22
N=56
N=86
N=64
N=44
N=106
N=81
ΔC 100 3 50 0 0 0 0
C0 0 0 50 0 3 10 100

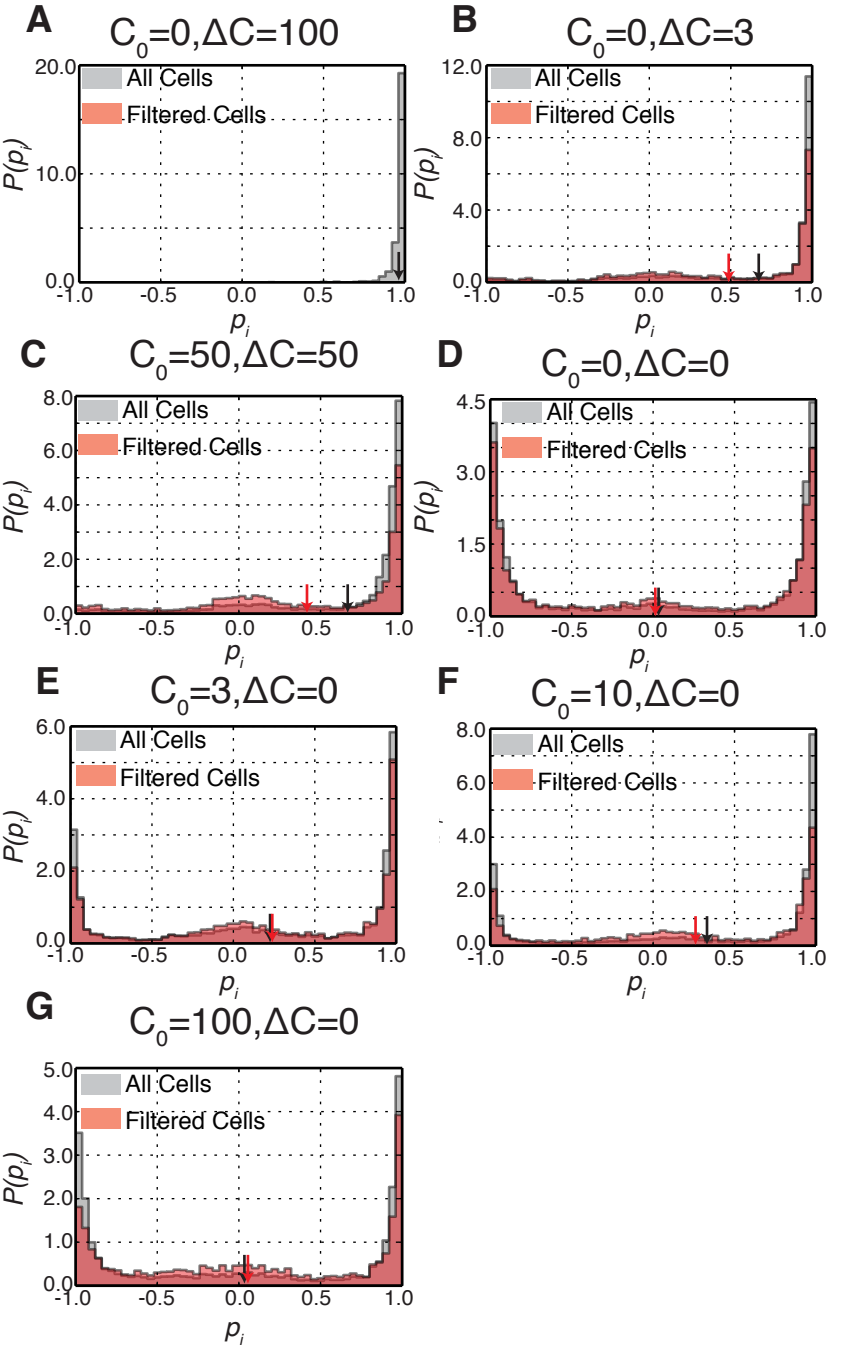
A
C0=0,ΔC=100
B
C0=0,ΔC=3
C
C0=50,ΔC=50
D
C0=0,ΔC=0
E
C0=3,ΔC=0
F
C0=10,ΔC=0
G
C0=100,ΔC=0
All Cells
Filtered Cells
P(pi)
pi

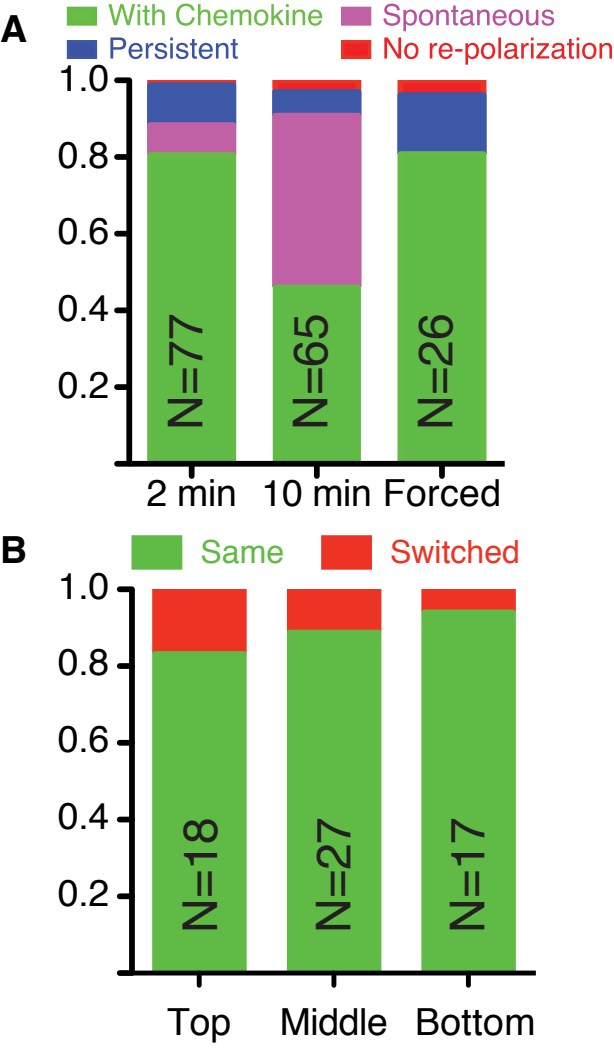
A
With Chemokine
Spontaneous
Persistent
No re-polarization
1.0
0.8
0.6
0.4
0.2
N=77
N=65
N=26
2 min
10 min
Forced
B
Same
Switched
1.0
0.8
0.6
0.4
0.2
N=18
N=27
N=17
Top
Middle
Bottom

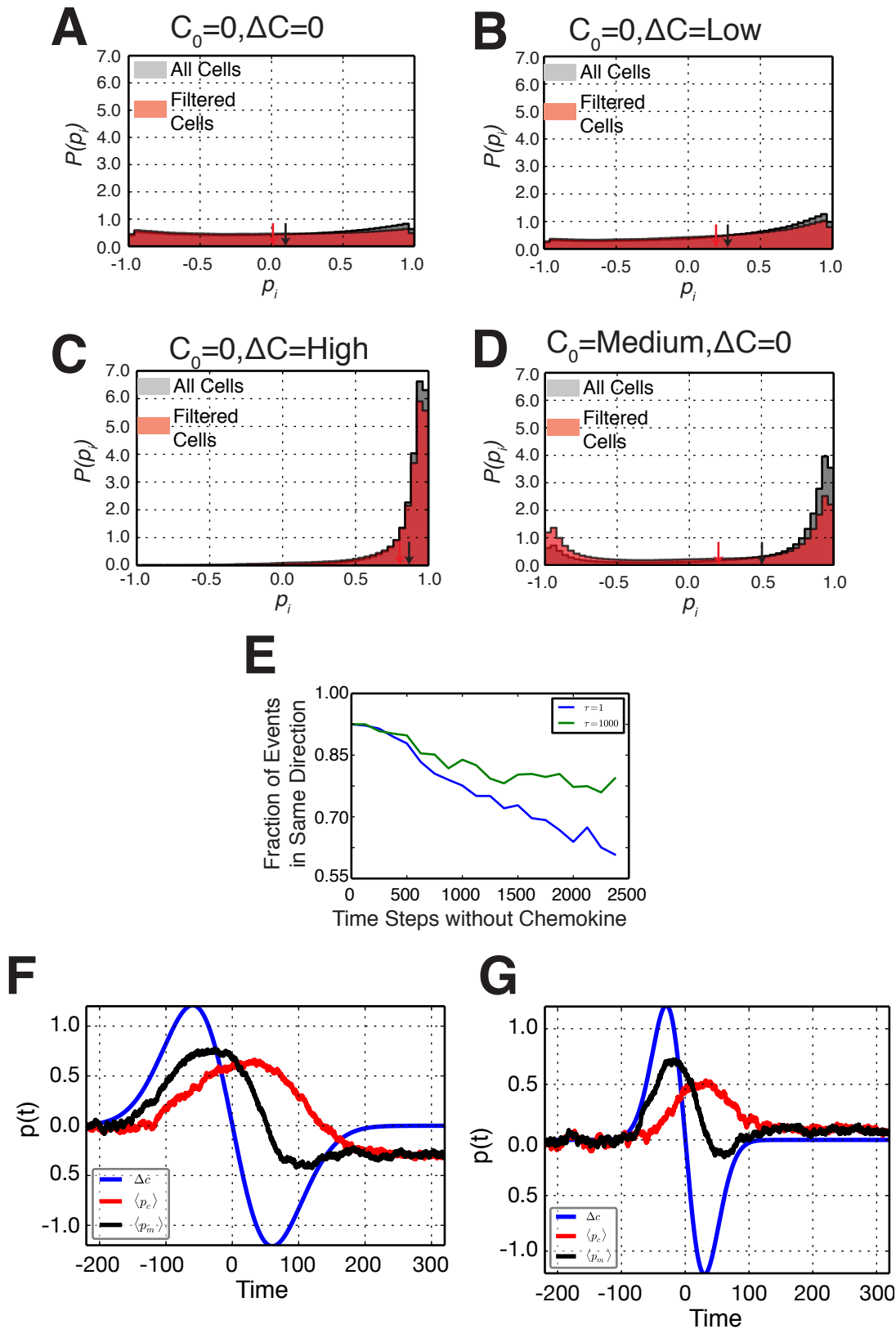
A
$C_0$=0,ΔC=0
All Cells
Filtered Cells
$P(p_i)$
$p_i$
B
$C_0$=0,ΔC=Low
C
$C_0$=0,ΔC=High
D
$C_0$=Medium,ΔC=0
E
Fraction of Events in Same Direction
Time Steps without Chemokine
$\tau$=1
$\tau$=1000
F
G
p(t)
Time
$\Delta c$
$\langle p_c \rangle$
$\langle p_m \rangle$

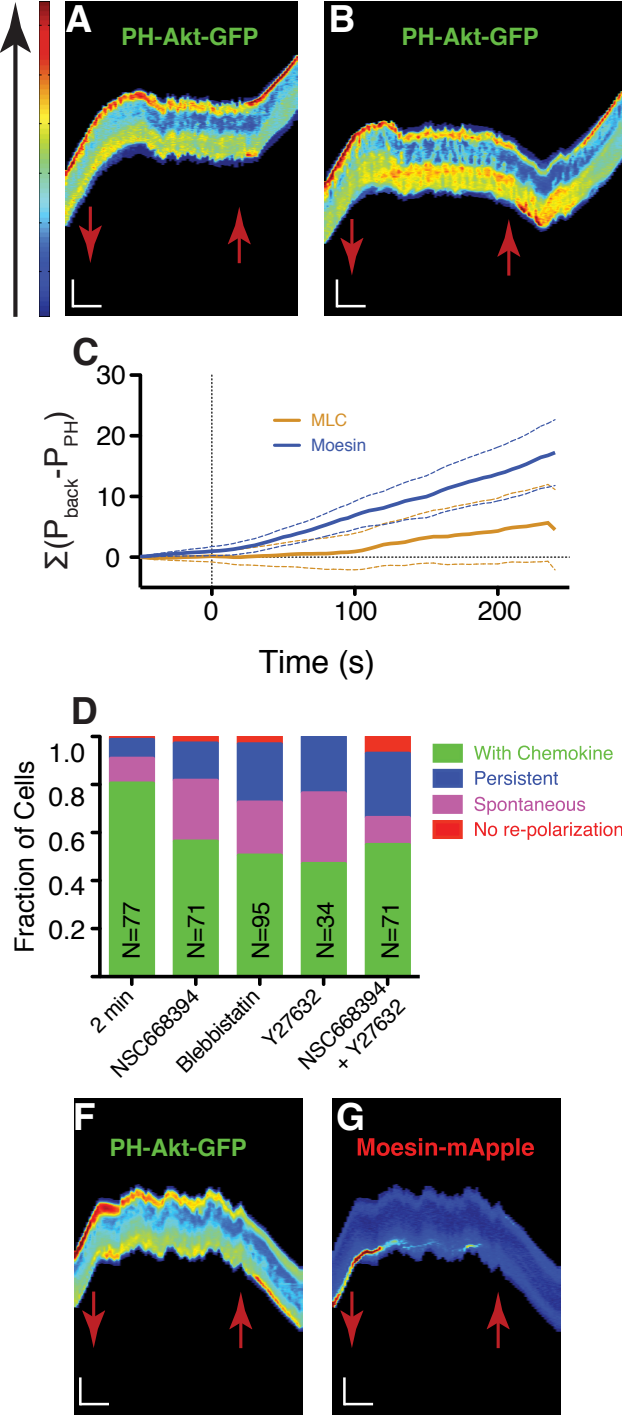
A
PH-Akt-GFP
B
PH-Akt-GFP
C
30
20
10
0
$\Sigma(P_{back}-P_{PH})$
MLC
Moesin
0
100
200
Time (s)
D
Fraction of Cells
1.0
0.8
0.6
0.4
0.2
N=77
N=71
N=95
N=34
N=71
With Chemokine
Persistent
Spontaneous
No re-polarization
2 min
NSC668394
Blebbistatin
Y27632
NSC668394 + Y27632
F
PH-Akt-GFP
G
Moesin-mApple

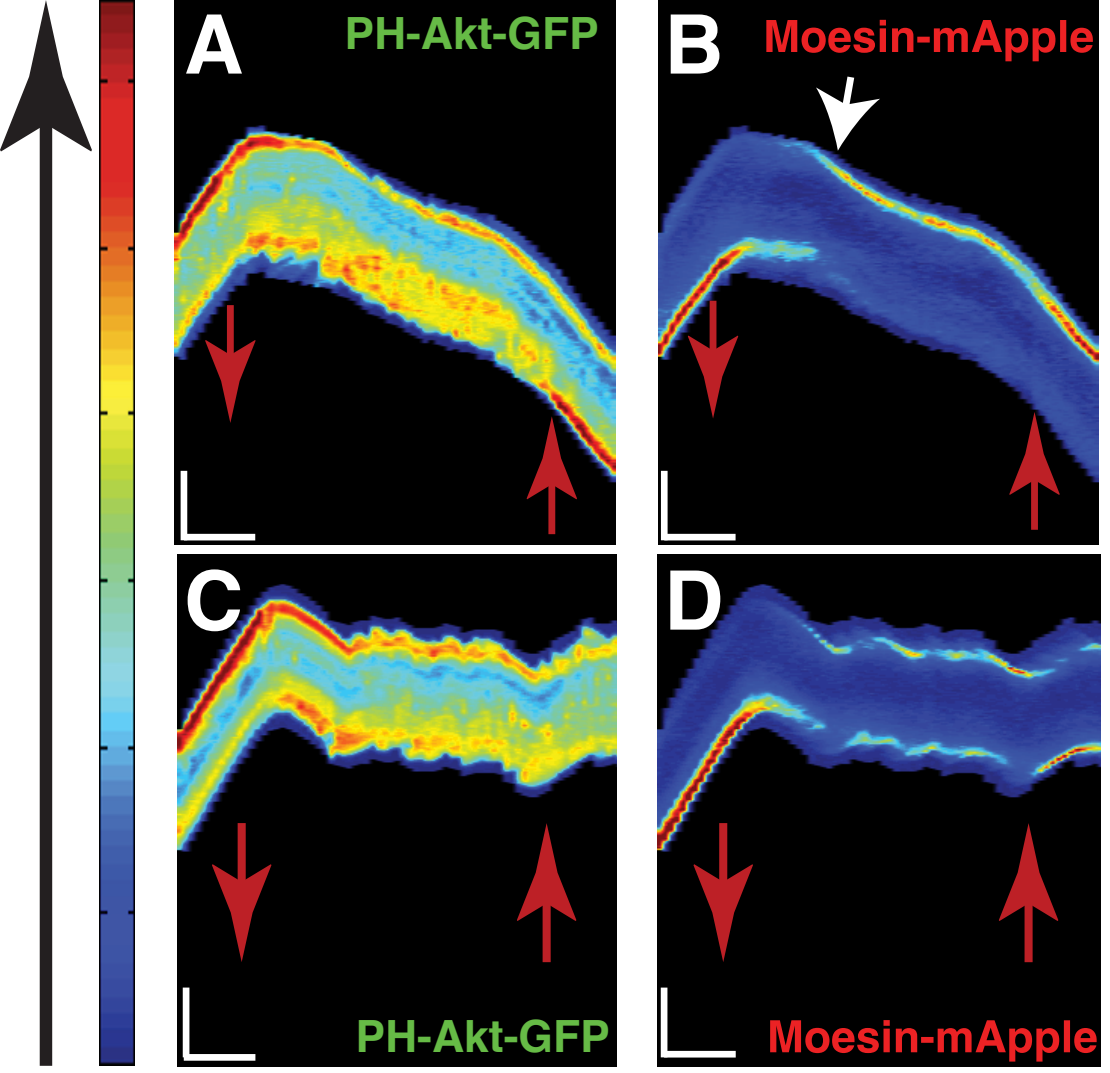
A
PH-Akt-GFP
B
Moesin-mApple
C
PH-Akt-GFP
D
Moesin-mApple

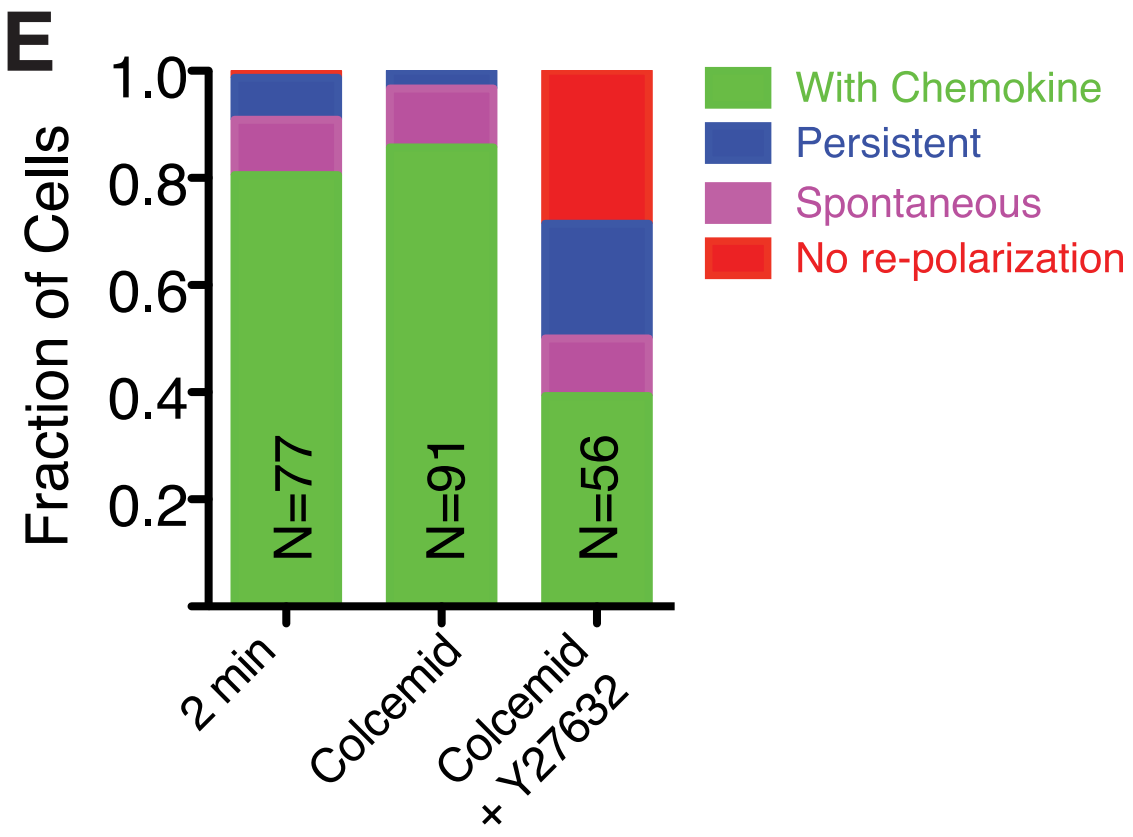
E
Fraction of Cells
1.0
0.8
0.6
0.4
0.2
N=77
N=91
N=56
2 min
Colcemid
Colcemid + Y27632
With Chemokine
Persistent
Spontaneous
No re-polarization

**Supplemental Figure Legends**

Figure S1: **Device design and cellular response to static chemical environments.** (**A**) Diagram of device geometry. Two inlet channels are used to introduce chemokine solutions into the device. The cell outlet channel is used when cells are introduced into the device from the outlet, downstream of the microchannel region. Insets demonstrate the positioning of the interface between the two inlet flows to balance pressure and maintain concentration difference across the microchannels. Fluorescein dye was used to visualize the separate streams. Inset shows a cell occluding a microchannel, resulting in build-up of chemokine in front, as well as a microchannel without a cell resulting in a gradient of dye along the length of the channel. (**B**, **E**, **H**, **K**) Montages of cells expressing PH-Akt-GFP in the conditions $C_0$=50 $\Delta C$=50 (**B**), $C_0$=3 $\Delta C$=0 (**E**), $C_0$=10 $\Delta C$=0 (**H**) and $C_0$=100 $\Delta C$=0 (**K**). (**C**, **F**, **I**, **L**) Kymographs of cells shown in montages. Kymographs are false-colored according to the color bar shown on the left to better visualize differences in PH-Akt intensity. Vertical scalebar: 15 μm. Horizontal scalebar: 100 seconds. (**D**, **G**, **J**, **M**) Plots of cell centroid and PH-Akt polarization for corresponding montages. (**N**) Fraction of persistently polarized (green) and not persistently polarized (red) in the static conditions tested. Vertical dashed were added to both kymographs and time plots to represent the time at which the cell was determined to have de-polarized.

Figure S2: **Histograms of instantaneous cell polarizations.** Given that the vast majority of cells were polarized at the start of the observation period we plotted the histogram of the entire trajectory (grey histogram) as well as the trajectory after the first depolarization event (red histogram) for all static conditions. While there was a shift in the first-depolarization histogram, even small chemotactic differences resulted in a strong bias toward the original direction. $C_0$=0 $\Delta C$=100 (**A**), $C_0$=0 $\Delta C$=3 (**B**), $C_0$=50 $\Delta C$=50 (**C**), $C_0$=0 $\Delta C$=0 (**D**), $C_0$=3 $\Delta C$=0 (**E**), $C_0$=10 $\Delta C$=0 (**F**), $C_0$=100 $\Delta C$=0 (**G**). Red and black arrows demonstrate the mean values for the two distributions in each condition.

Figure S3: **Cellular responses to dynamics change in chemokine**. (**A**) Percentage of cells that did not depolarize upon removal of chemokine (Persistent) or depolarized upon removal of chemokine and either repolarized upon reintroduction of chemokine (Normal), re-polarized prior to reintroduction of chemokine (Spontaneous) or did not depolarize (No re-polarization). (**B**) Cells were separated by whether they were in the bottom, middle or top third of the microchannel, relative to the end at which they entered. As can be seen, the directional memory of the cells was not dependent on the position of the cell in the microchannel.

Figure S4: **Histograms of simulated cell polarizations**. Histograms of simulated cellular polarizations including all polarization measurements (grey) and only those that occurred following the first depolarization of a cell (red) for the conditions $C_0$=0 $\Delta C$=0 (**A**), $C_0$=0 $\Delta C$=Low (**B**), $C_0$=0 $\Delta C$=High (**C**), $C_0$=Medium $\Delta C$=0 (**D**). (**E**) Directional re-polarization statistics for simulated cells as a function of

the amount of time between removal and reintroduction of chemokine for two parameters of the timescale of the memory kernel: smaller timescale with $\tau$=1 in blue, and a larger timescale with $\tau$=1000 in green. The larger timescale exhibits longer memory compared to the smaller timescale, with a higher fraction of cells repolarizing in the same direction at any time. (**F**) For slow waves, where the timescale of the positive gradient $\tau_{\Delta n}$ = 200 is larger than the timescale of the memory kernel $\tau_{pc}$,=100, the polarization of the membrane switches directions as seen by the final negative p(t) at long times. (**G**) For faster waves, where $\tau_{\Delta n}$ = 100 is comparable to $\tau_{pc}$, the cell exhibits directional memory, and does not switch polarization directions as seen by the positive p(t) at long times. Details found in the main text.

Figure S5: **Identification of long-lived cytoskeletal polarization**. (**A**, **B**) Kymographs of PH-Akt-GFP localization for cells expressing either MLC-mApple (**A**) or moesin-mApple (**B**), shown in Figure 5 (**A**) and (**C**), respectively. Red arrows mark the time when chemokine was removed (down) and reintroduced (up). Vertical scalebar: 15 μm. Horizontal scalebar: 100 seconds. (**C**) Cumulative sum of the difference between either MLC or moesin polarization and PH-Akt polarization. (**D**) Responses of cells to removal and reintroduction of chemokine (as described in Figure S3) for the different drugs and drug combinations tested. (**E**, **F**) Kymographs of PH-Akt-GFP (**E**) and moesin-mApple (**F**) for a cell treated with moesin inhibitor NSC668394.

Figure S6: **Microtubule disruption alters relaxation dynamics of moesin polarization**. (**A**, **B**) Kymographs of PH-Akt-GFP (**A**) and moesin-mApple (**B**) for a cell dynamically exposed to the microtubule inhibitor colcemid. Red arrows mark the time when chemokine was removed (down) and reintroduced (up). Vertical scalebar: 15 μm. Horizontal scalebar: 100 seconds. (**C**, **D**) Kymograph of PH-Akt-GFP (**C**) and moesin-mApple for a cell exposed to the combination of colcemid and Y27632 (**D**). Red arrows mark the time when chemokine was removed (down) and reintroduced (up). Vertical scalebar: 15 μm. Horizontal scalebar: 100 seconds. (**E**) Responses of cell to removal and reintroduction of chemokine (as described in Figure S3) for treatment both with colcemid alone as well as drug combinations including colcemid.

**Supplementary Movie Legends**

Movie S1: Movie of cell shown in Figure 1A ($\Delta C$=100 $C_o$=0). Scalebar: 10 μm

Movie S2: Movie of cell shown in Figure 1D ($\Delta C$=3 $C_o$=0). Scalebar: 10 μm

Movie S3: Movie of cell shown in Figure 1G ($\Delta C$=0 $C_o$=0). Scalebar: 10 μm

Movie S4: Movie of cell shown in Figure S1B ($\Delta C$=50 $C_o$=50). Scalebar: 10 μm

Movie S5: Movie of cell shown in Figure S1E ($\Delta C$=0 $C_o$=3). Scalebar: 10 μm

Movie S6: Movie of cell shown in Figure S1H ($\Delta C$=0 $C_o$=10). Scalebar: 10 μm

Movie S7: Movie of cell shown in Figure S1K ($\Delta C$=0 $C_o$=100). Scalebar: 10 μm

Movie S8: Movie of cell shown in kymograph in Figure 3B, repolarizing in the same direction up reintroduction of chemokine. Chemokine was removed at t=0 and reintroduced at t=85. Scalebar: 10 μm.

Movie S9: Movie of cell shown in kymograph in Figure 3B, repolarizing in the opposite direction up reintroduction of chemokine. Chemokine was removed at t=0 and reintroduced at t=115. Scalebar: 10 μm.

Movie S10: Movie of cell shown in kymograph in Figure 5A, expressing PH-Akt-GFP (green) and MLC-mApple (red). Chemokine was removed at t=0 and reintroduced at t=300. Scalebar: 10 μm.

Movie S11: Movie of cell shown in kymograph in Figure 5C, expressing PH-Akt-GFP (green) and hsMoesin-mApple (red). Chemokine was removed at t=0 and reintroduced at t=320. Scalebar: 10 μm.

Movie S12: Movie of cell shown in kymograph in Figure 5F,G, expressing PH-Akt-GFP (green) and hsMoesin-mApple (red), and treated with the ROCK inhibitor Y27632. Chemokine was removed and drug introduced at t=0 and the chemokine was reintroduced and the drug removed at t=260. Scalebar: 10 μm.

Movie S13: Movie of cell shown in kymograph in Figure S5F,G, expressing PH-Akt-GFP (green) and hsMoesin-mApple (red), and treated with the ezrin inhibitor NSC668394. Chemokine was removed and drug introduced at t=0 and the chemokine was reintroduced and the drug removed at t=300. Scalebar: 10 μm.

Movie S14: Movie of cell shown in kymograph in Figure 5A,B, expressing PH-Akt-GFP (green) and hsMoesin-mApple (red), and treated with the microtubule depolymerizer colcemid. Chemokine was removed and drug introduced at t=0 and the chemokine was reintroduced and the drug removed at t=265. Scalebar: 10 μm.

Movie S15: Movie of cell shown in kymograph in Figure 5C,D, expressing PH-Akt-GFP (green) and hsMoesin-mApple (red), and treated with both colcemid and Y27632. Chemokine was removed and drug introduced at t=0 and the chemokine was reintroduced and the drug removed at t=250. Scalebar: 10 μm.